J. Fluid Mech. (1986), vol. 163, pp. 195–226
Printed in Great Britain

Rayleigh–Bénard convection in an intermediate-aspect-ratio rectangular container

By PAUL KOLODNER, R. W. WALDEN, A. PASSNER AND C. M. SURKO

AT&T Bell Laboratories, Murray Hill, New Jersey 07974

(Received 24 April 1985 and in revised form 12 August 1985)

We report a study of the flow patterns associated with Rayleigh–Bénard convection in rectangular containers of approximate proportions $10 \times 5 \times 1$ at Prandtl numbers σ between 2 and 20. The flow is studied at Rayleigh numbers ranging from the onset of convective flow to the onset of time dependence; Nusselt-number measurements are also presented. The results are discussed in the content of the theory for the stability of a laterally infinite system of parallel rolls. We observed transitions between time-independent flow patterns which depend on roll wavenumber, Rayleigh number and Prandtl number in a manner that is reasonably well described by this theory. For $\sigma \lesssim 10$, the skewed-varicose instability (which leads directly to time dependence in much larger containers) is found to initiate transitions between time-independent patterns. We are then able to study the approach to time dependence in a regime of larger Rayleigh number where the instabilities in the flow are found to have an intrinsic time dependence. In this regime, the onset of time dependence appears to be explained by the recent predictions of Bolton, Busse & Clever for a new set of time-dependent instabilities.

1. Introduction

Pattern formation and time dependence in non-equilibrium dissipative systems are problems of considerable interest, both from a practical point of view and as unsolved problems in many-body physics. A classic example of such a system is convection in a horizontal fluid layer heated from below (i.e. Rayleigh–Bénard convection). This system is particularly appealing since, from a theoretical point of view, the fluid equations which describe the system are well known, and, from an experimental viewpoint, the boundary conditions on the fluid can be well controlled. Although there has been extensive theoretical and experimental work on this problem, many questions still remain to be answered.

Consider the evolution of such a system as the temperature difference (in dimensionless units the Rayleigh number R) across the fluid layer is increased. Convection begins at some threshold Rayleigh number R_c; below this value there is no flow, and the heat is transmitted by conduction through the fluid. For the rectangular containers discussed here, the first spatial pattern above R_c is confirmed both experimentally and theoretically to be a stationary system of parallel rolls. As R is further increased, this flow pattern can evolve quasi-statically, or it can become intrinsically time dependent. At sufficiently large R, the flow eventually becomes turbulent. If R is raised quickly above R_c, other (metastable) flow patterns can be induced. These details of pattern selection and time dependence are known to depend on the shape and dimensions of the container (i.e. the aspect ratios, which are ratios

of the lateral extent to the height of the container) and on the Prandtl number σ (which is the ratio of the viscosity to the thermal diffusivity of the fluid) (see Behringer, Gao & Shaumeyer 1983; Bergé 1981; Busse & Whitehead 1971; Gollub & Benson 1980). The dependence of pattern selection and time dependence on these parameters is as yet not well understood.

In this paper we report a study of pattern formation in rectangular containers of approximate aspect ratio 10×5 in an environment where the boundary conditions are as well controlled as possible. The evolution of the fluid flow is studied as a function of Rayleigh number until persistent time dependence (in contrast to transient rearrangements of the flow pattern) is observed. By studying convection in a container of aspect ratio which is finite but not small, we are able to study facets of pattern formation and time dependence which either do not occur or are masked by other effects in containers of different geometry. The work presented here is part of a larger effort to understand the dynamics of a convecting fluid in the time-dependent regime. Since there is considerable evidence that the details of the spatial pattern of the flow strongly influence the time-dependent phenomena (Gollub & Benson 1980; Behringer *et al.* 1983), it is important to understand the spatial flow pattern in detail.

The choice of aspect ratio Γ of the convection containers discussed here was motivated by two considerations. For small containers (e.g. $\Gamma \lesssim 5$), changes in the flow pattern are severely restricted by the boundaries, and the flow becomes time dependent in a manner which is similar to that observed in dynamical systems of low dimensionality (Gollub & Benson 1980; Maurer & Libchaber 1980; Dubois & Bergé 1980). It seems unlikely that the dynamics in these systems is closely related to the dyanamics in larger fluid systems. On the other hand, for large systems (e.g. $\Gamma \gtrsim 20$), the initial time dependence is typically a slow motion of the roll pattern on the timescale of the horizontal-diffusion time (Gollub, McCarriar & Steinman 1982). This slow motion makes it difficult to distinguish clearly other changes and instabilities in the pattern. Thus our choice of aspect ratio was motivated by the desire to have a container sufficiently large that one could observe changes in the spatial flow pattern well before the onset of chaotic time dependence, but small enough so that the parallel container boundaries would inhibit slow wandering of the rolls. One advantage of this choice is that a container of aspect ratio 10×5 is easier to maintain in a well-controlled thermal environment than a container of a very large aspect ratio. A disadvantage is that this regime is more difficult to treat theoretically, since the infinite-aspect-ratio calculations are significantly modified by the finite lateral dimensions of the container.

Much intuition about changes in the spatial pattern of the flow has come from calculations of the stability of uniform periodic rolls in a laterally infinite fluid layer. Since the number of parameters which describe the evolution of the flow pattern is large (i.e. including the Prandtl number, the Rayleigh number, and the initial state of the flow), even the infinite-aspect-ratio case poses a formidable problem (Busse 1978). The stability of parallel-roll convection is illustrated in figures 1 and 2, where the stability boundaries are shown as a function of Rayleigh number and roll wavenumber α† for Prandtl numbers 3.5 and 15 respectively (Busse & Clever 1979; Clever & Busse 1974; Busse 1978; Bolton, Busse & Clever 1983; Busse & Whitehead 1971, 1974). Below the heavy solid line in each figure there is no fluid motion. In the shaded regions in Rayleigh-number and wavenumber space, convection in a pattern of straight parallel rolls is stable. Beyond these regions, parallel-roll convection is

† The wavenumber α is defined as $\alpha = 2\pi d/\lambda$, where d is the height of the fluid layer and λ is the repeat distance of this pattern of parallel rolls.

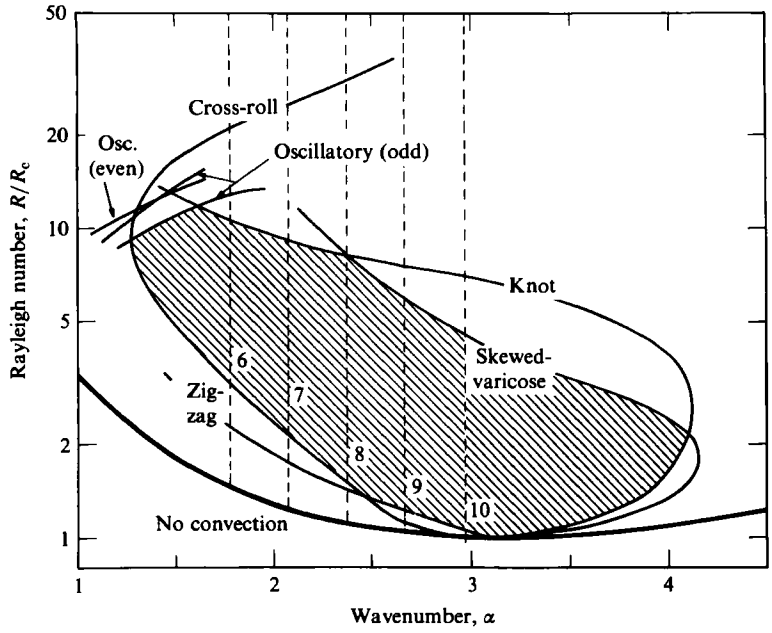

FIGURE 1. Stability diagram for a convection pattern of straight parallel rolls of wavenumber α for Prandtl number 3.5 assuming infinite lateral boundary conditions. This pattern is stable in the shaded region. The vertical dashed lines indicate the quantization of mean roll wavenumber by the finite aspect ratio of container A (cf. table 1). The numbers indicate the number of rolls parallel to the short side of the container. *Note.* The calculated stability boundaries presented in this paper are interpolated and extrapolated from the calculations of Busse, Bolton, and Clever (Busse & Clever 1979; Busse 1978; Bolton, Busse & Clever 1983; and private communications). Although the curves presented should be qualitatively correct, uncertainties of 10–20% are possible in some cases.

unstable to the various instabilities indicated by the lighter solid lines. It can be seen by comparing figures 1 and 2 that these instability boundaries have a significant Prandtl-number dependence. In contrast to the case of infinite aspect ratio, one important effect of a container of finite aspect ratio is that it must contain an integral number of rolls. To a first approximation (i.e. assuming constant wavelength), this means that the wavenumber α is quantized. In figures 1 and 2 the dashed vertical lines identify the mean wavenumbers corresponding to the integral number of rolls in our experimental containers.

Assuming for a moment that the theory is unmodified for a container of finite aspect ratio, we would expect that beyond the stability boundaries an initial flow pattern of parallel rolls would change; however, prediction of the final state of the flow is beyond the scope of this linear theory. For example, as shown in figure 1, a state with nine parallel rolls at a Rayleigh number of 7 is unstable to the skewed-varicose instability. Possible stable states of the system at this Rayleigh number include flow patterns with 6, 7 or 8 parallel rolls. However, whether transitions to such states actually occur and, if so, the likelihood of their occurrence is not known. The experiments described in this paper show that the system prepared in this way does, in fact, evolve to stable, time-independent states of either 7 or 8 rolls.

As another example of pattern evolution, consider for Prandtl number 3.5 (figure 1) a stable pattern of six rolls at Rayleigh number of $9R_c$. As R is further increased, the system of parallel rolls becomes unstable for all wavenumbers at about $13R_c$. Our experiments show that as a function of increasing R the pattern of parallel rolls first

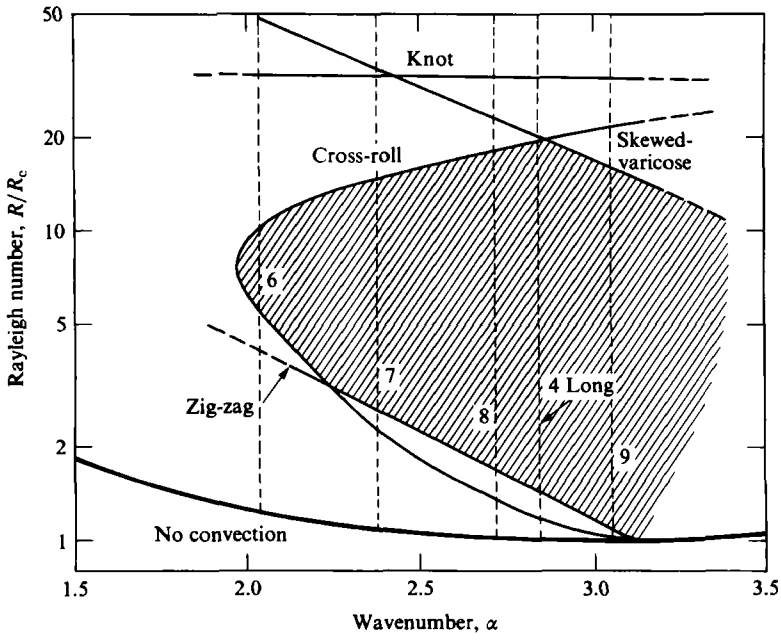

FIGURE 2. Stability diagram for a convection pattern of straight parallel rolls of wavenumber α for Prandtl number 15 assuming infinite lateral boundary conditions. This pattern is stable in the shaded region. The vertical dashed lines indicate the quantization of mean roll wavenumber by the finite aspect ratio of container B (cf. table 1). The numbers indicate the number of rolls (parallel to the *short* side of the container, except as noted). (See *note*, figure 1.)

becomes distorted and then becomes time-dependent. The time dependence can be qualitatively understood in the context of recent theoretical predictions by Bolton, Busse & Clever (1983) for a set of modes in this range of wavenumber and Rayleigh number. These calculations predict an oscillatory instability at discrete frequencies which are multiples of the characteristic frequency of circulation of a fluid element around a roll.

As illustrated in figure 2 for a Prandtl number of 15, a different sequence of instabilities is encountered as the Rayleigh number is increased above R_c. At a wavenumber corresponding to nine rolls, the skewed-varicose instability is encountered at $R \approx 17R_c$. For fewer rolls, the first boundary encountered above R_c is that of the cross-roll instability. It is this instability which is known to trigger bimodal convection (Busse & Whitehead 1971) at $R \gtrsim 10R_c$. The resulting fluid flow is a superposition of secondary rolls located in the boundary layer and oriented at right angles to the initial roll pattern. We will find that the initial roll pattern is still evident in the presence of bimodal convection, and that we can continue to study the stability of this roll pattern as R is further increased (e.g. to Rayleigh numbers large enough to encounter the skewed-varicose and knot instabilities).

The remainder of the paper is organized in the following manner. The apparatus for the present experiments is described in §2. In §§3 and 4 we discuss the fluid parameters and experimental procedures used in these experiments. The experimental results are described in two parts: results for Prandtl numbers $\sigma < 10$ are discussed in §5.1, and for $10 < \sigma < 20$ in §5.2. Finally, in §6 we present a discussion of these results, relating them to current theoretical models and to results from other experiments.

2. Apparatus

2.1. *General arrangement*

The convection apparatus, which provides a radiation-shielded vacuum environment for the convection container, together with associated optical systems, sits on a vibration-isolated optical table. Other associated equipment is mechanically decoupled from the table. The laboratory temperature is maintained constant to ± 1 °C, permitting reasonable stability of the optical and electronic component systems. A minicomputer handles data acquisition and many of the control and system monitoring functions, and a digital image-processing system aids flow-pattern analysis.

2.2. *Convection apparatus and temperature-control systems*

2.2.1. *Environment for the convection container*

In order to provide a suitable environment for high-precision heat-transport measurements together with simultaneous visual observations, careful attention has been given to thermal isolation of the convection container. Precision temperature regulation and radiation shielding are achieved by the use of five independent temperature measurement and control systems. The convection container and radiation shields are placed in an evacuated box for additional thermal isolation (cf. figure 3). The working fluid is contained between a 6.4 mm thick copper bottom plate and a sapphire top plate with horizontal walls of acrylic plastic or of glass. The temperature of the top plate of the container is controlled by water flowing from a bath circulator, regulated in three stages to better than ± 0.001 °C, short and long term. The temperature of the cooling water is monitored continuously by a quartz thermometer probe (10^{-4} °C sensitivity) which provides an absolute temperature reference during calibration. Since the quartz thermometer is not tied to the regulation systems, it also provides an independent indication of noise or drift in water temperature during an experimental run. The container is surrounded by a copper box thermally linked to the circulating cooling water (and thus maintained at a temperature close to that of the container top plate). Windows at the top and sides of the copper box, each consisting of a sapphire plate glued to an infrared-absorbing glass plate and thermally clamped at the edges to the copper box, shield against radiative heat transfer when temperatures inside and outside the box are substantially different. There is an independently regulated copper shield around the bottom plate of the convection container which is maintained within ± 0.01 °C of the bottom-plate temperature by feedback from a d.c. bridge using a matched pair of thermistors – one mounted on the container bottom plate and the other on the radiation shield. Similarly, a matched pair of thermistors is used to maintain the temperature of the top plate of the copper box (and the window mounted in it) at the temperature of the container top plate.

The copper box is contained in a stainless-steel box with side and top windows of anti-reflection-coated glass, evacuated to a pressure of < 5 μm Hg (typically ≈ 2 μm), maintained by a nitrogen cold trap in series with a standard diffusion pump. This pressure is well below the estimated pressure, for which the mean free path of remaining gas molecules is comparable to the container dimensions.

Optical access from the top of the apparatus allows for visualization of the entire flow pattern, usually by a shadowgraph technique. Similarly, visual access from the sides permits observation of a horizontal view of the flow pattern. Images of the flow pattern are projected on to a screen and recorded on video tape. An image-processing

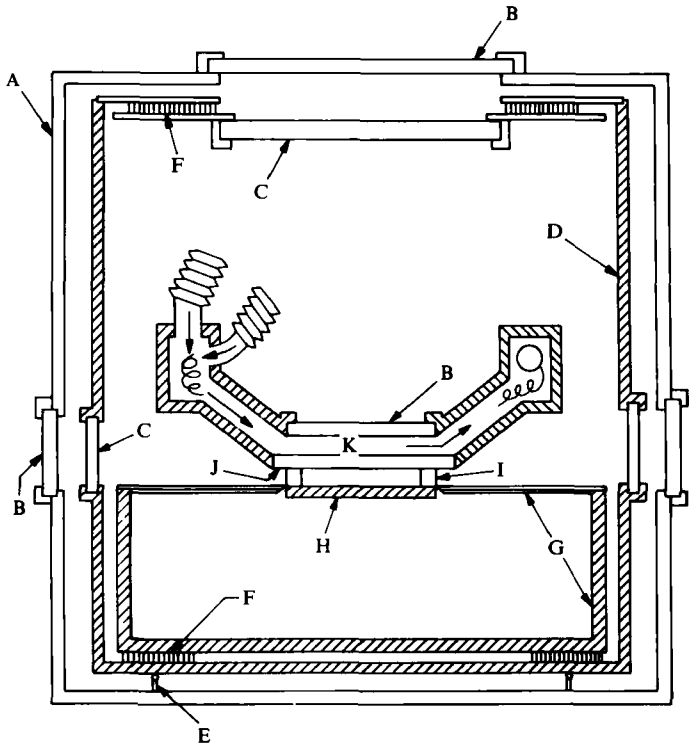

FIGURE 3. Flow visualization and heat transport apparatus. A, stainless-steel box, evacuated to $\approx 10^{-3}$ torr. B, anti-reflection-coated glass windows. C, infrared-absorbing glass sandwiched with sapphire (for thermal-radiation shielding). D, gold-plated copper radiation shield. E, support post: nylon peg and glass bead. F, thermoelectric heat exchangers. G, radiation shield for bottom plate of container. H, bottom plate of the convection container. I, walls of the convection container (acrylic or glass). J, sapphire top plate of the convection container. K, flowing water (from external bath circulator).

system is used to enhance the contrast of the video images, either in real time or from (time-lapse) video tapes.

2.2.2. *Rayleigh–Bénard containers*

The container is constructed from a copper bottom plate and sapphire top plate, with interchangeable glass or plastic walls. The copper bottom plate is illustrated in figure 4(*a*). A heater constructed of non-inductively wound nichrome wire (with total resistance of about 300 Ω) is sandwiched with a thin layer of epoxy between two copper plates. The upper section of the bottom plate is 4.7 mm thick and has a highly polished gold-plated surface in contact with the fluid. Two holes of 0.25 mm diameter located near opposite ends of the container allow for filling and draining of the container through 0.25 mm i.d., 0.5 mm o.d. stainless-steel capillary tubes. Ten thermistor probes are mounted at various positions about 0.4 mm below the polished surface of the bottom plate. Reference resistors for each thermistor are mounted on the 1.5 mm thick bottom plate of the sandwich.

The walls are made as a rectangular frame (wall thickness 5.0 mm) of Plexiglas (container A) or of precision-ground and polished glass (container B). The top plate of the container is a sapphire plate, 4.8 mm thick, epoxied into the cooling-water channel. There is an O-ring groove in the top surface of the copper sandwich and

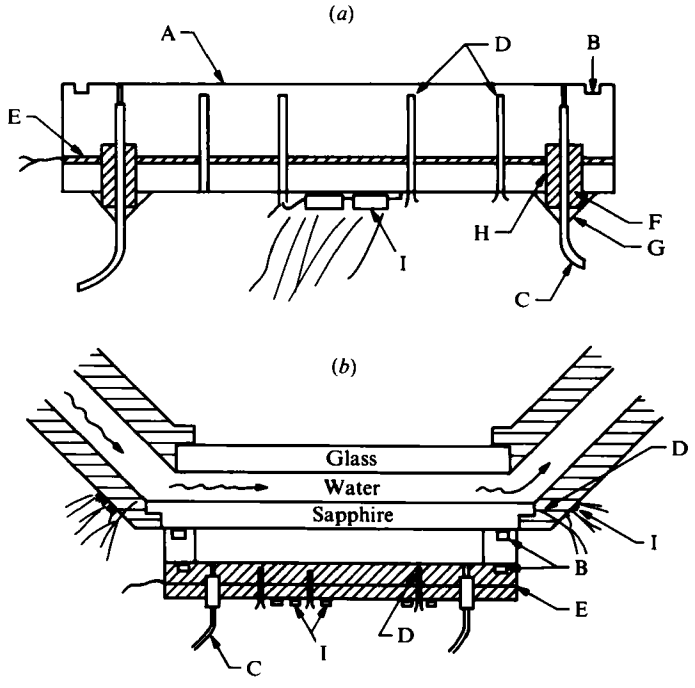

FIGURE 4. Convection container construction. (*a*) Bottom plate; (*b*) container assembly. A, gold-plated mirror surface. B, O-ring groove. C, stainless-steel capillary fill tube. D, thermistor. E, nichrome wire heater in epoxy layer. F, brass tubing. G, hard solder. H, epoxy seal. I, metal-film reference resistor.

	Aspect ratios			
Container	Γ_L	Γ_W	d [cm]	Wall material
A	10.61	5.32	0.461	Acrylic
B	9.25	4.42	0.525	Glass

TABLE 1. Convection containers

around the top surface of each of the wall frames. The container is clamped together by a spring-tensioned supporting frame of low thermal conductance. Container dimensions are given in table 1 and thermal properties of the wall materials in table 2.

2.2.3. *Temperature measurement and regulation*

There are five independent temperature-regulation systems in the experiment as discussed above, and two additional temperature-measurement systems. A refrigerated bath circulator (5 l/min circulation rate) regulates the cooling water temperature to a stability of ± 0.1 °C over our operating range of between 10° and 80 °C. The water passes through an additional mixing chamber (cf. figure 5) with approximately a 50 s thermal time constant, and then past a heater which is controlled by feedback from a thermistor in a d.c. bridge circuit. The thermistor is mounted a few cm ahead of the inlet-tube fitting of the experimental chamber. The temperature of the water at this point is stable to ± 0.001 °C for short times ($\lesssim 1$ min) and to ± 0.010 °C for longer times ($\gtrsim 1$ h).

Material	Thermal conductivity[1, 2, 4, 5] at 25 °C [erg/cm s °C]	Thermal diffusivity[2, 3, 4, 5] at 25 °C [cm²/s]
Copper	4.01×10^7	1.16
Sapphire	4.6×10^6	0.151
Acrylic	2.0×10^4	1.1×10^{-3}
Glass	9.5×10^4	4.7×10^{-3}

[1] Thermal conductivity of acrylic from K. Eiermann & K. H. Hellwege, *J. Polymer Sci.* **57**, (1962), 102.

[2] Thermal properties of the glass provided by the manufacturer, Hellma Cells, Inc. (West Germany).

[3] Thermal diffusivity of acrylic from H. R. Simonds, A. J. Weith & M. H. Bigelow, *Handbook of Plastics*, 2nd edn, D. van Nostrand Co., New York, 1949.

[4] Thermal properties of copper from *Handbook of Chemistry and Physics*, 41st edn (ed. C. D. Hodgnor), Chemical Rubber Publishing Co., Cleveland, Ohio, 1959.

[5] Thermal properties of sapphire from *Thermophysical Properties of Matter, Vol. 2* (ed. Y. S. Touloukian), Plenum, 1970.

TABLE 2. Thermal properties of convection containers

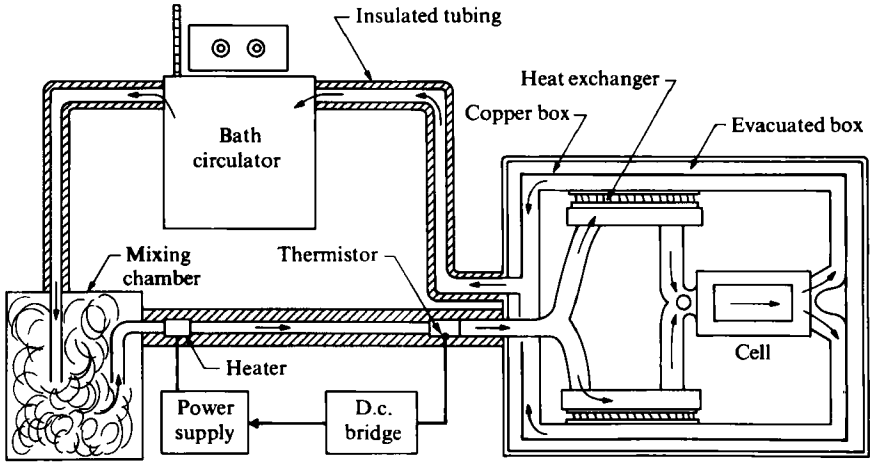

FIGURE 5. Cooling-water circulation system.

A third stage of regulation is provided inside the experimental chamber of an a.c. bridge circuit. The incoming water flows through the temperature-regulated side of a thermoelectric heat exchanger, then across the sapphire top plate of the container and into a rectangular copper tube anchored to the copper box which shields the container. The copper tube provides a heat sink for the heat exchanger, which serves to fine-tune the temperature of the water flowing across the container. The input signal for this regulation is provided by one of six thermistors which are mounted in a row, embedded in the flow channel immediately adjacent to the upstream edge of the sapphire plate and about 0.5 mm below the flowing water (cf. figure 4*b*). Two metal-film reference resistors are mounted on the copper surface adjacent to each thermistor. The two resistance values were chosen to give optimum sensitivity for different temperature ranges. By mounting the resistors adjacent to the respective thermistors the very small temperature dependence of the metal-film resistors was

automatically incorporated into the calibration. The 0.5 mm diameter glass-probe thermistors were mounted with thermal grease and monitored by a five-wire a.c. bridge circuit (cf. Mueller, Ahlers & Pobell 1976). A similar set of sensors was mounted on the downstream side of the sapphire plate.

While one thermistor was used to regulate the water temperature, any of the other thermistors could be monitored by a second a.c. bridge. For large heat flux through the container (from the heater embedded in the container bottom plate), the temperature change δT between incoming and outflowing water was consistent with the heat capacity of the flowing water. Typically the temperature rise was $\approx 0.2\,\%$ of the vertical temperature difference across the container ΔT ($\lesssim 0.001$ °C at $R = R_c$; i.e. of the order of magnitude of typical random fluctuations and drift in the cooling-water temperature); and $\delta T/\Delta T \lesssim 0.7\,\%$ at maximum heat input. However, at large values of heat flux the heat transfer through the sapphire and copper was better than transfer into the cooling water, so the regulation system suppressed the temperature of the incoming cooling water by a few millidegrees (about 0.008 °C/W) below the thermistor temperature. Apart from some of the calibration tests the second a.c. bridge was used to monitor one of the thermistors in the container bottom plate. The quartz thermometer probe, which was mounted directly in the flowing water about 4 cm upstream from the regulation thermistors, provided absolute-temperature readings as well as an independent check of regulation stability.

2.3. *Optical systems*

The optical system used for flow visualization by vertical and horizontal shadowgraphy is sketched in figure 6. A 25 mW He–Ne laser is expanded to 100 mm diameter and collimated with an adjustable telescope. The beam is divided by a 50/50 beamsplitter; half of the output is sent horizontally through the container, and half is directed vertically on to the container from above. As the vertical beam passes through the convecting fluid, both before and after its reflection in the polished bottom plate of the container, it is refracted by the lateral gradients in optical index of the fluid. These gradients are produced by the non-uniform lateral convective temperature profile. Thus, light rays which pass through cold, dense, decending fluid are sightly focused, while those in warm regions are defocused. The image projected on to a screen placed in the optical path some distance away from the container exhibits a pattern of dark and light regions which delineate the regions of vertical flow (the convective roll boundaries). As shown in figure 6, two images of the vertical shadowgraph pattern were formed. For weak flow patterns just above R_c an optical path length of 2.7 m from the container to the viewing screen was useful. For flow patterns at $R \gtrsim 10R_c$, this pattern was substantially distorted, so a beamsplitter was used to form a second shadowgraph image at a distance 1.4 m from the container, which was displayed on the same screen.

As mentioned above, a fraction of the laser beam is also directed horizontally through the container, in a direction parallel to its shorter sides. The shadowgraph thus formed is displayed and recorded along with the two vertical shadowgraphs. This horizontal shadowgraph is useful for examining the flow pattern as a function of depth in the fluid, especially when the flow is in the form of straight rolls parallel to the short sides of the container.

The three shadowgraph images are recorded, along with numerical data in an LED display, by a high-resolution video camera. Video tapes of the images are analysed using the digital image-processing system described below.

It is useful to point out that shadowgraphs do not necessarily yield *local*

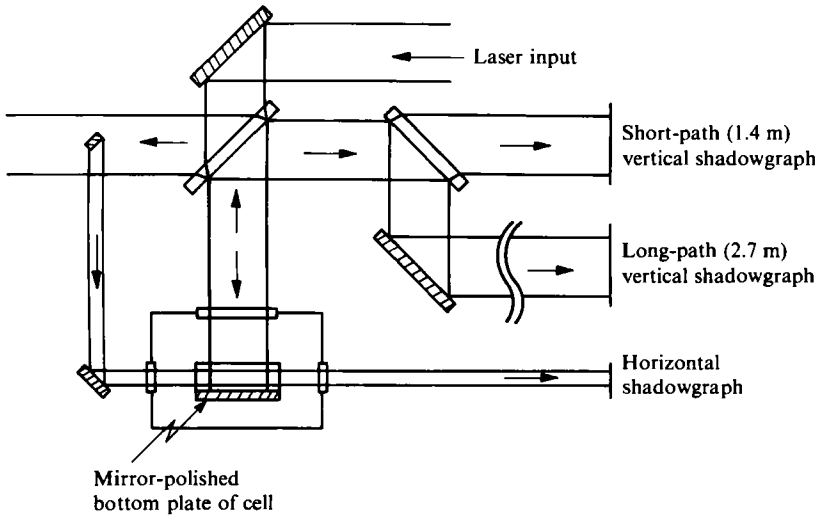

FIGURE 6. Optical system for flow visualization by shadowgraphy.

information, especially in the far field. The intensity at a given point in the image may include contributions from light rays deflected from strongly refracting regions distant from the corresponding point in the fluid. Truly localized information about the flow can only be obtained from light-scattering techniques such as LDV, or by tomographic techniques, such as multiple-path interferometry.

2.4. *Video system and image processing*

The shadowgraph images produced using the techniques described above are viewed with an RCA high-resolution video camera, displayed in real time on a video monitor, and recorded on VHS format $\frac{1}{2}$ in. videotape casettes. Because of the long timescales associated with these experiments, we typically record five-second segments made at two-minute intervals. This mode of sampling is usually adequate to allow us to monitor all relevant transitions in the convective flow patterns. At moderate and high Reynolds numbers, the image contrast and noise levels on the videotape are sufficient to allow us to clearly identify these patterns. At low R, however, this is not the case, and the image contrast is dominated by visual artifacts unrelated to the flow pattern. In order to eliminate these artifacts and enhance the contrast in the convective flow pattern, we have installed a Digital Graphics System CAT-1631 digital image-processing system. The front end of this system can perform 8-bit digitization of a full 512×512 pixel video image at video rates (30 frames/s). The size of the image of our convection container is adjusted to fill approximately 140×200 pixels, and each frame contains all three of the shadowgraphs described in the previous section. We have developed a menu-type software system which allows us to interactively perform colour coding, picture arithmetic, spatial averaging, statistics, and a limited range of geometric transformations. These operations can also be called in software programs. One such program allows identification of the flow pattern in an image of a weakly convective state by subtracting from it an image of the container made just below the onset of convection. This background-free image is then rescaled for maximum contrast. This program allows identification of a videotaped convective pattern at values of R down to $\approx 1.05 R_c$. More sophisticated algorithms utilizing

multi-frame averaging, background normalization and spatial convolution allow pattern recognition for $(R-R_c)/R_c \gtrsim 0.01$, using live images.

2.5. *Computer systems*

Most of the data acquisition and experimental control, and some monitoring functions were performed by a PDP 11/23 minicomputer, while data processing and analysis were accomplished by a time-shared VAX 11/780 computer, hardwired to the lab minicomputer. Under the supervision of the PDP 11/23, the voltage across the container heater was set by a Fluke Model 4275A 4-terminal power supply; heater current was monitored by use of a Hewlett–Packard Model 3456 multimeter which could also be used to measure the (four-terminal) heater resistance as a cross-check for determining heater power. A multichannel analog-to-digital converter served to digitize the a.c. bridge offset which is a measure of the bottom-plate temperature.

3. Definition of the parameters and fluid properties

We use L, W, and d respectively to denote the container length, width and height. The major and minor aspect ratios are then $\Gamma_L = L/d$ and $\Gamma_W = W/d$. The kinematic viscosity is $\nu = \eta/\rho$ and the thermal diffusivity is $\kappa = \Lambda/\rho c_p$, where Λ is the thermal conductivity, ρ is the fluid density, c_p is the heat capacity per unit mass at constant pressure and η is the shear viscosity. The Prandtl number is $\sigma = \nu/\kappa$.

The Nusselt number N is the ratio of the effective heat transport of the fluid relative to transport due to the (static) conductivity alone. Thus, below the critical Rayleigh number $N = 1$; above the critical Rayleigh number $N = \Lambda_{\text{eff}}/\Lambda$, where Λ_{eff} takes into account heat transport due to both conduction and convection.

The Rayleigh number is defined by $R = g\alpha_p \Delta T d^3/\kappa\nu$, where g is the acceleration of gravity, α_p is the coefficient of thermal expansion at constant pressure, and ΔT is the temperature difference across the fluid. The critical Rayleigh number for the onset of convection depends in general on the smallest horizontal dimension of the container. For a laterally infinite container $R_c = 1708$. For a rectangular container of aspect ratio 5×10, the critical Rayleigh number is increased by about 1.3 %.† Hereafter we define $R_c = 1708$, rather than the experimental onset of convection, in order to facilitate quantitative comparison with theory.

Since the relevant properties of our working fluids – water and ethanol – have been extensively studied, the tabulated values of these properties available from standard reference works have been used in the computation of Rayleigh and Nusselt numbers. Some fluid properties at selected temperatures are presented in table 3.

4. Procedure

Our experimental measurements were designed to determine Rayleigh and Nusselt numbers as a function of time at fixed heater power while recording the corresponding flow pattern. This section describes our experimental procedure, the initiation of particular flow patterns and considerations concerning the computation of Nusselt and Rayleigh numbers from the raw data.

† This was estimated by computer calculations based on the amplitude equations for our specific aspect ratio (Greenside & Coughran 1984; and M. C. Cross, H. J. Greenside & J. Tesauro, private communication).

Fluid temp. [°C]	Density [g/cm³] ρ[1,2]	Specific heat [erg/g C] C_p[3,4]	Thermal conductivity [erg/cm s C] A[5,6]	Kinematic viscosity [cm²/s] ν[7-9]	Thermal diffusivity [cm²/s] κ	Prandtl number σ	Coeff. of thermal expansion [C^{-1}] α_p[10,11]	Thermal diffusion time [s] $\tau_v = d^2/\kappa$ (Cell B)	ΔT_c [°C] (Cell B)
				Ethanol					
10	0.7978	2.318×10^7	1.709×10^4	0.0181	0.9238×10^{-3}	19.59	1.058×10^{-3}	281.3	0.2077
30	0.7808	2.480	1.649	0.0128	0.8518	15.04	1.108	305.1	0.1294
50	0.7633	2.673	1.590	0.0092	0.7792	11.77	1.185	335.1	0.0775
				Water				(Cell A)	
30	0.99568	4.171×10^7	6.035×10^4	0.008039	1.453×10^{-3}	5.532	0.3038×10^{-3}	146.3	0.6834
50	0.98807	4.190	6.365	0.005558	1.537	3.615	0.4554	138.3	0.3335
70	0.97781	4.222	6.695	0.004163	1.622	2.568	0.5880	131.1	0.2040

[1] Ethanol: *International Critical Tables of Numerical Data for Physics, Chemistry and Technology* (ed. E. W. Washburn), vol. 3, p. 27. McGraw-Hill, New York 1928. ρ from four-parameter fit, as given in reference; estimated uncertainty: 0.01 %.

[2] Water: *International Critical Tables*, vol. 3, pp. 24–26. ρ interpolated from tabulated data; estimated uncertainty: ~ 10 p.p.m.

[3] Ethanol: *Thermophysical Properties of Matter* (ed. Y. S. Touloukian), vol. 6, p. 180. Plenum Press, New York 1970. C_p from four-parameter fit as given in the reference; estimated uncertainty: 0.3 %.

[4] Water: *International Critical Tables*, vol. 5, p. 113, and vol. 7, p. 232. C_p interpolated from tabulated data; estimated uncertainty: 0.05 %.

[5] Ethanol: *Thermophysical Properties of Matter*, vol. 3, p. 169. A from two-parameter fit essentially as given in reference; estimated uncertainty: 2.4 %.

[6] Water: *International Critical Tables*, vol. 5, p. 218. A from 2-parameter fit provided in the reference; estimated uncertainty: 0.1 %.

[7] ν is computed from ρ (notes 2, 3) and η (notes 9, 10) using $\nu \equiv \eta/\rho$.

[8] Ethanol: *Handbook of Chemistry and Physics*, 41st edn (ed. C. D. Hodgnon), p. 2184. Chemical Rubber Publishing Co., Cleveland, Ohio, 1959. η from four-parameter fit to reference data; estimated uncertainty: 0.5 %.

[9] Water: *International Critical Tables*, vol. 5, p. 10. η interpolated from tabulated data; estimated uncertainty: 0.01 % below 40 °C; 0.5 to 1.0 % above 40 °C.

[10] Ethanol: I. Klesper, *Zeitschrift für Physikalische Chemie*, Neue Folge **51**, 1 (1966). α_p from three-parameter fit to the reference data; estimated uncertainty: 0.6 %.

[11] Water: α determined from a smoothed interpolation of the density data; estimated uncertainty: 0.05 %.

TABLE 3. Fluid parameters. Estimated errors are indicated above for the measured parameters. Other fluid parameters included in Rayleigh-number calculations are derived from these. Estimated standard deviation in Rayleigh number due to uncertainty in the fluid properties is about 3 % for ethanol and about 0.1 % for water at 30 °C, rising to 1 % at 80 °C.

4.1. *General procedure*

For all the measurements reported here, the top plate of the container was maintained at constant temperature by regulation of the cooling water. Changing the cooling water temperature by a few degrees or more requires changing the bath circulator setting and adjusting the d.c. bridge for temperature regulation within a few millidegrees of the desired operating point. When the d.c. bridge output has stabilized, the a.c. bridge associated with the heat exchangers inside the intermediate copper box is adjusted until the quartz thermometer reading remains within ± 0.001 °C of the desired value.

After a change in the circulating-water temperature, the system was allowed to equilibrate for at least several hours and, if necessary, small readjustments were made in the bridge settings before data collection began. Once the system had stabilized, the quartz-thermometer reading was observed to be steady to within ± 0.001 °C with respect to the a.c. bridge setting. Even after large transients the system returned to within ± 0.001 °C, implying excellent stability for both the quartz thermometer and the a.c. bridge.

The usual experimental procedure under computer control was to increase the bottom-plate heater power Q_h slowly in discrete steps, waiting for equilibrium after each step. For an initial survey run at a given σ, steps in R were taken at 30- to 60-min (10 t_v–25 t_v where t_v is the vertical thermal diffusion time) intervals. The a.c. bridge readings, corresponding to the container-bottom-plate temperature, were monitored continuously by chart recorder and sampled by the computer at time intervals (typically 18 s) short compared with the vertical thermal diffusion time.

When the survey run encountered a transition which might be affected by the step size or rate, the transition was repeated with much smaller steps and longer time at each step. For most runs, time-lapse videotape records supplemented the computer-data records. The numerical identification displayed in the video image allowed the videotape records to be correlated in detail with the computer data.

4.2. *Nusselt-number measurements*

Accurate determination of the Nusselt and Rayleigh numbers required attention to both carefully measuring and minimizing sources and sinks of heat. Thermal shielding and evacuation of the apparatus minimized external convective and radiative heat flow. The major contributions to the bottom-plate heating were the 4-terminal wire-wound heater [Q_h], the thermistors (one in a d.c. bridge [Q_d], and usually one in an a.c. bridge circuit [Q_a]), and heating from the 15 mW He–Ne laser used for shadowgraphy [Q_l].

Heating due to the a.c. bridge thermistor was negligible ($\approx 4\ \mu$W). Heating due to the d.c. bridge thermistor was strongly temperature-dependent (but accurately calibrated) and was typically $\approx 100\ \mu$W. The laser heating was also small ($\approx 200\ \mu$W) with a slow variation over several months as the laser aged. By comparison, about 15–80 mW was required to reach R_c for these experiments. The 4-terminal measurements of heater power were accurate to an estimated ± 0.1 %.

The bottom plate of the container was well radiation-shielded from the upper (and colder) part of the apparatus. Heat transfer laterally through the sidewalls – due to radiation – was small at low Rayleigh numbers and assumed to be negligible. However, the container walls and the supporting frame provided a heat path parallel to the fluid. For example, heat transfer through the glass walls was about 80 % of that through the water for $R < R_c$.

The thermal conductivity of the walls was determined for purposes of Nusselt-number determination using the measured thermal conductivity and temperature dependence of the wall material and estimating the effective wall area in contact with the upper and lower container boundaries. This effective area is less than the actual wall cross-section because of the O-rings and O-ring grooves at the contact surfaces. This (one constant) value of effective area was chosen to give constant N for $R < R_c$ at all operating temperatures. In fact, there was a slight increase in the effective thermal conductivity of the walls after the container was filled, probably due to fluid filling the inner side of the O-ring grooves and effecting better heat transfer between the container wall and the sapphire plate.

The thermal conductivity of the copper bottom plate (about 660 times that of water) was sufficient to allow neglect of lateral gradients; and, indeed, thermistor measurements detected no lateral gradient except at very high Rayleigh number. However, the finite thermal conductivity of the sapphire top plate (about 50 times that of water) is not completely negligible. The maximum temperature difference across the sapphire can be estimated from the measured heat flux and the known thermal conductivity of the sapphire. However, because the sapphire plate is larger than the convection container and because of the finite thermal conductivity of the container walls, the temperature of the sapphire surface which contacts the fluid in the convection container is non-uniform. The vertical temperature difference across the sapphire at R_c is approximately 1 % of R_c. For the case of water with plastic walls, the temperature of the lower surface of the sapphire at the edges of the container is larger relative to the temperature of the sapphire at the centre of the container by about 0.5 % of R_c at R_c. For the case of ethanol with glass walls, the temperature at the edges is depressed relative to the centre by about the same amount (i.e. 0.5 % of R_c at R_c).

4.3. *Determination of Rayleigh number*

Computation of Rayleigh number depends on the fluid properties and the temperatures at the top and bottom of the container. The temperature at the bottom of the container is determined directly from thermistor measurements, while the temperature at the top of the container (i.e. at the lower surface of the sapphire plate) must be determined indirectly in the process of Nusselt-number computation. Since the fluid properties are temperature dependent, there are small gradients in the properties between the bottom and top of the container. The mean temperature at the half-height of the container was chosen for the determination of fluid properties for computation of Rayleigh number. This choice removes, to first order, the dependence of R_c and $\mathrm{d}N/\mathrm{d}R|_{Rc^+}$ on departures from the Boussinesq approximation (Busse 1967*a*; Ahlers 1980; Walden & Ahlers 1981). Departures from the Boussinesq approximation, as indicated by Busse's (1967*a*) parameter P, are small for these experiments. Specifically, $P \lesssim 0.20$ at $R = R_c$ in all cases, so that the results should not differ noticeably from a Boussinesq system (Ahlers 1980; Walden & Ahlers 1981).

4.4. *Initiation of flow patterns*

The initiation of the various symmetric flow patterns employed in these experiments was accomplished in most cases by simple exploitation of the fluid and container properties. One method of pattern initiation relies on the difference in thermal diffusivity between the container walls and the working fluid. For example, the thermal diffusivity of the glass wall (container B) is greater than that of ethyl alcohol. Thus, if the container is heated from below while the top remains at constant temperature, the rapid diffusion of heat through the walls causes the adjacent water

to be heated more rapidly than the remaining fluid; fluid near the walls begins moving upward, resulting in a symmetric pattern of eight rolls.† Conversely, the thermal diffusivity of water is greater than that of acrylic. Therefore, if the water is heated from below while the top remains at constant temperature, the favoured pattern for container A is 10 rolls, with downward flow at the container boundaries.

On a few occasions, a heating lamp projector with a mask was used momentarily to initiate a specific flow pattern. Since the strong influence of lateral boundaries prohibits the growth of arbitrary patterns, only patterns which are reasonably stable near R_c can be initiated by heat lamp. A lamp projection mask was chosen to generate a perturbation which favours the selection of the desired flow pattern.‡

5. Experimental observations

For essentially all of the temperatures reported here, the independent variable was the bottom-plate-heater power Q_h. Imposition of constant Q_h (rather than constant Rayleigh number) permits high precision in heat-flux measurements. Previous studies have indicated that there is no significant difference in behaviour of the fluid system for constant heat flux or constant Rayleigh number in our operating regime (e.g. Gao & Behringer 1984; Walden 1983).

While Q_h was held constant at a precisely measured value (or was increased quasi-statically), the temperature of the bottom plate was monitored and recorded, and the top-plate temperature was held fixed. At constant Q_h, Rayleigh number varies inversely with the Nusselt number. Although Rayleigh number is used as if it were an independent variable in §§5 and 6, it should be understood that both Nusselt and Rayleigh numbers vary slightly at constant heat flux during a transition in flow pattern or other time-dependent behaviour. In such cases the Rayleigh numbers presented here are approximate or average values, and it is expected that similar behaviour would occur if the Rayleigh number were held fixed and Q_h were allowed to vary.

5.1. *Experiments for small Prandtl number* ($2 < \sigma < 10$)

As indicated above, for container A (aspect ratio 10.6×5.3) the stable pattern at onset of convection obtained by increasing R sufficiently slowly was always 10 rolls parallel to the short side of the container. Similarly, for container B (9.3×4.4), the initial stable pattern was 8 rolls parallel to the short side of the container. Typical experimental results for small σ are illustrated schematically in figure 7 for $\sigma = 3.5$. Beginning with 10 rolls and heating slowly, the pattern is stable, and the rolls are essentially uniform in size for $R < 6R_c$. Above $6R_c$ the pattern begins to deform with increasing R (but remains time independent at constant R). Finally, a critical Rayleigh number $R_s = 6.5R_c$ is reached above which the (deformed) 10-roll pattern is no longer stable. Figures 7 (*d*)–(*g*) illustrate the break-up of a pair of rolls at constant heat flux. The

† The wavenumber dependence of the critical Rayleigh number for the infinite-aspect-ratio case (figure 2) would appear to imply that a pattern of nine rolls should be favoured near R_c. In practice, however, although a nine-roll pattern has been observed in container B, it is more difficult to achieve than the symmetric eight-roll pattern.

‡ Chen & Whitehead (1968), for example, used a similar technique for initiating patterns in large-aspect-ratio containers. They employed a rectangular grid to generate patterns of a specific wavenumber. In general, simple rectangular grids (of any orientation or spacing) were found to select the same flow pattern as no grid at all (i.e. uniform heating); effective masks for our experiments were usually those which provided intense heat to small areas of the container.

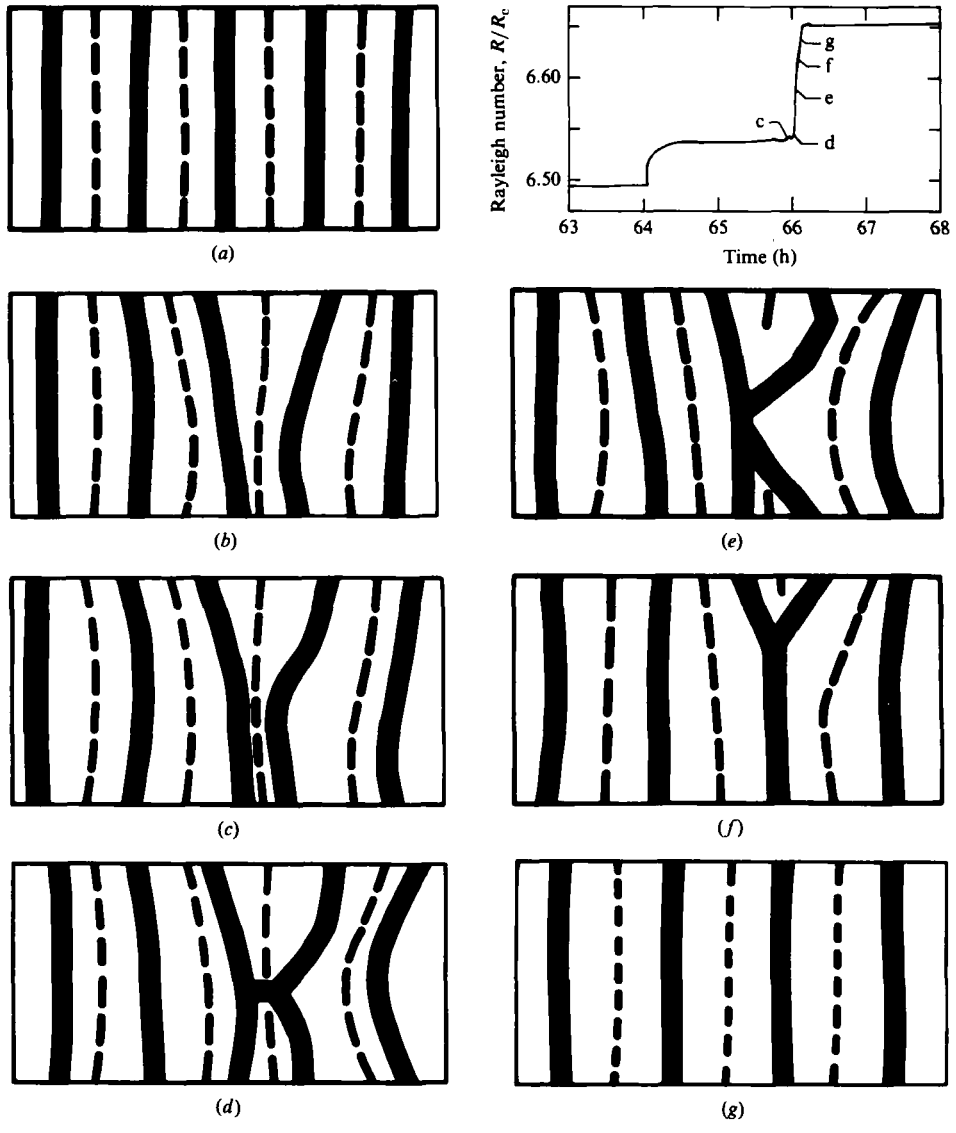

FIGURE 7. Schematic representation of a transition in flow pattern from 10 to 8 rolls in container A for water at $\sigma = 3.5$. Solid lines: upflow boundaries; dashed lines: downflow boundaries. Time is measured from the onset of convection. (*a*) $R = 4.5\,R_c$, $t = 2{:}15$ (h:min); (*b*) $6.45\,R_c$ at 43:00; (*c*) $6.542\,R_c$ at 65:56; (*d*) $6.544\,R_c$ at 66:01; (*e*) $6.588\,R_c$ at 66:03; (*f*) $6.617\,R_c$ at 66:05; (*g*) $6.637\,R_c$ at 66:07.

Inset: Rayleigh number *versus* time near the transition. The first rise in R follows a 0.62 % increase in heater power. The larger increase in R two hours later (at *constant heat flux*) is due to the flow-pattern transition.

Nusselt number decreases monotonically by about 1.8 % during this transition to an 8-roll pattern.

As shown in figure 8, the 8-roll pattern is stable until $R \gtrsim 10R_c$. Again, the pattern begins to distort above $10R_c$ (figure 8*b*); then another pair of rolls break up at around $12R_c$ (figures 8*c–e*) while the heat flux is maintained constant, resulting in a pattern of 6 rolls. With further increase in Rayleigh number the flow becomes time-dependent

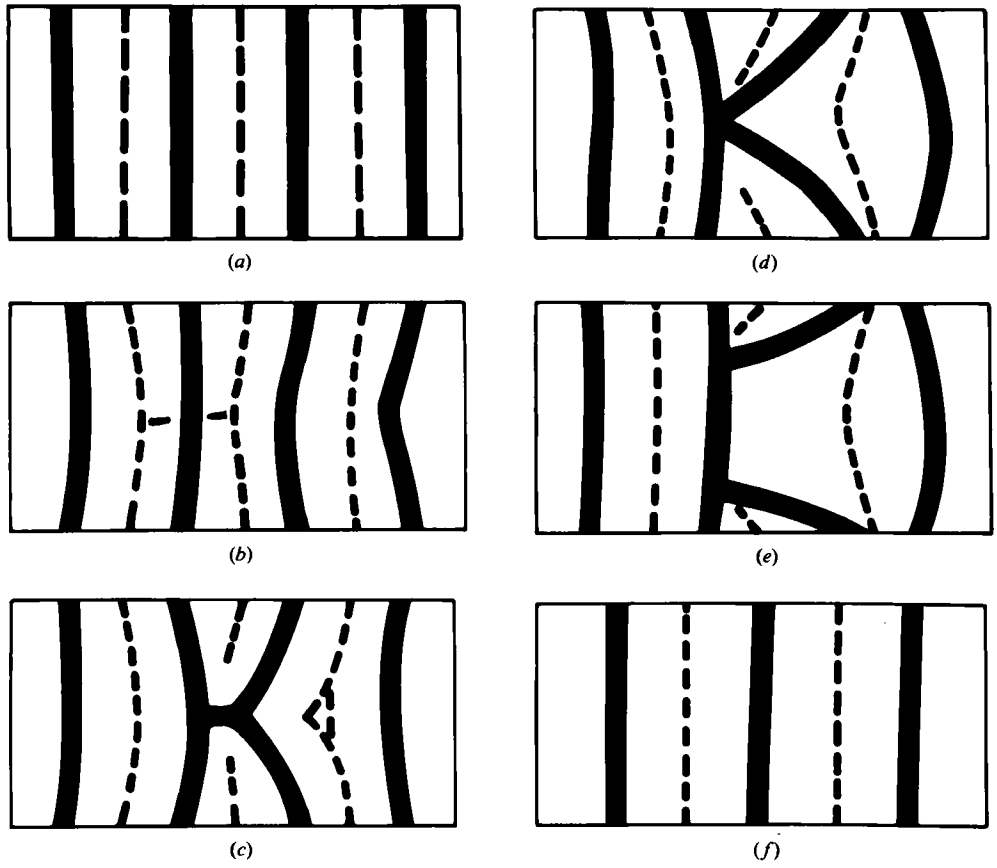

FIGURE 8. Schematic representation of a transition in flow pattern from 8 to 6 rolls in container A for water for $\sigma = 3.5$. Time is measured from the transition from 10 to 8 rolls. (*a*) $R = 10.2\,R_c$, $t = 3{:}20$ (h:min); (*b*) $12.38\,R_c$ at 7:16; (*c*) $12.39\,R_c$ at 7:25; (*d*) $12.49\,R_c$ at 7:26; (*e*) $12.60\,R_c$ at 7:27; and (*f*) $12.83\,R_c$ at 7:40.

near $18R_c$. The nature of this time dependence has been described in detail elsewhere (Walden *et al.* 1984); however, the underlying 6-roll pattern is still evident at much higher Rayleigh numbers (i.e. $R > 40R_c$).

If the Rayleigh number is now reduced quasi-statically, the 6-roll pattern remains stable until $R \approx 9R_c$. Below $9R_c$ a 'T-shaped' roll is formed at one (or sometimes both) ends of the container (figure 9). We call this a 'soft' pattern in the sense that the mean roll wavenumber (averaged over the two-dimensional pattern) can be varied continuously by stretching or squeezing the 'T'. As Rayleigh number is reduced towards R_c, the 'soft' 6-roll pattern remains, but the mean roll wavelength gradually decreases.

Figure 10 is a plot of Nusselt number *versus* Rayleigh number for the case $\sigma = 5.5$. Heat transport is a maximum for rolls of nearly square cross-section for R near R_c, and the maximum moves to larger wavenumber α with increasing R (Busse 1967*b*). Thus the successive transitions $10 \rightarrow 8 \rightarrow 6$ rolls which reduce α with increasing R are accompanied by drops in Nusselt number.

Sometimes a transition may involve the destruction of a single roll rather than a pair of rolls. This is illustrated in figure 11. The removal of a single roll always occurs along one of the end boundaries of the container (a topological necessity), whereas

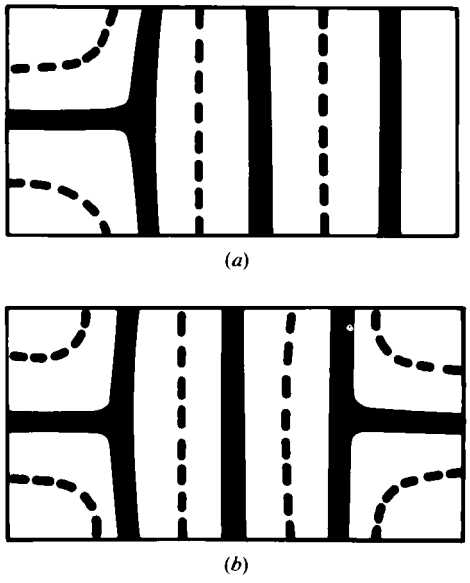

FIGURE 9. Single and double 'soft' patterns which appear with decreasing Rayleigh number.

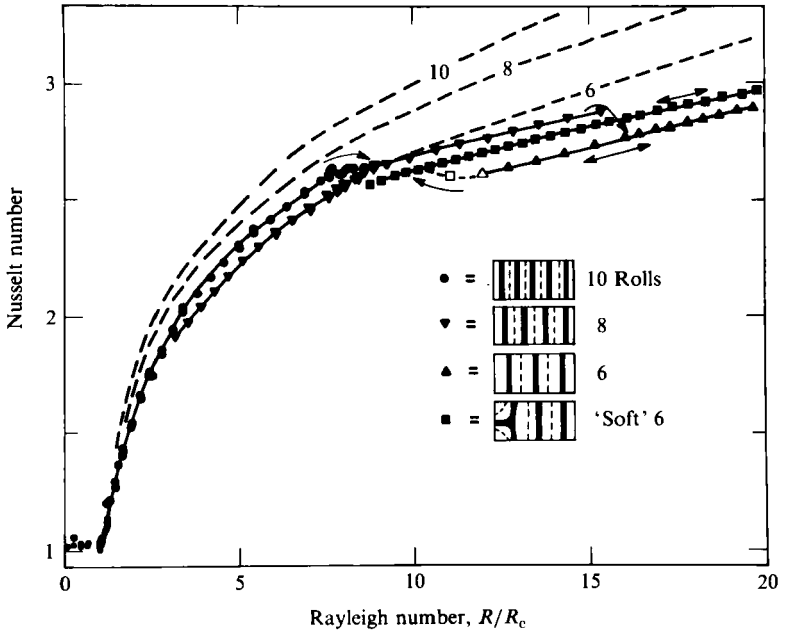

FIGURE 10. Nusselt number as a function of Rayleigh number measured for different convective patterns in container A for $\sigma = 5.5$. The dashed lines (corresponding to patterns of 10, 8 and 6 parallel rolls) are from theory which assumes infinite lateral boundary conditions (Clever & Busse 1974; see also *note*, figure 1).

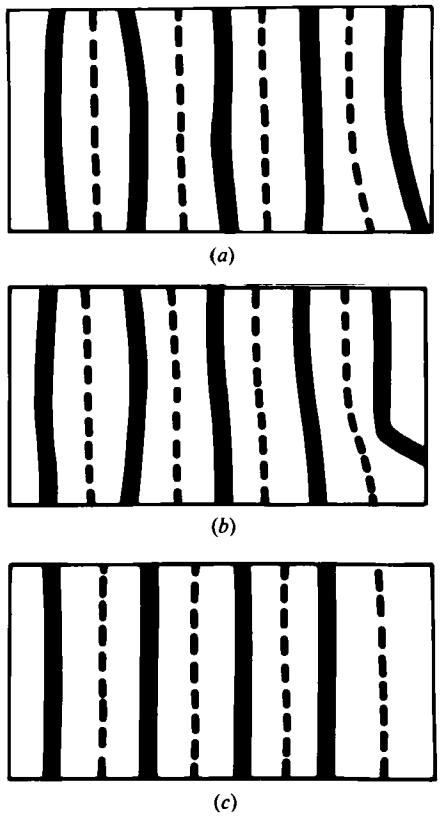

FIGURE 11. Schematic representation of a typical transition from 10 to 9 rolls.

the removal of a pair of rolls occurs in the interior of the flow, i.e. away from the ends.

The same sequence of transitions (e.g. $10 \rightarrow 8 \rightarrow 6$, or $10 \rightarrow 9 \rightarrow 7$) is observed consistently for repeated tests at a given σ, and the Rayleigh number of the transition is well defined and repeatable, with sufficiently small $\mathrm{d}R/\mathrm{d}t$. (The details of the transition, e.g. the choice of which roll pair is dissolved, are variable from one trial to another, however.) In one instance a transition did not result in a stable pattern of parallel rolls. For $\sigma = 3.0$, beginning with a 9-roll pattern, a complicated but reproducible transition was observed which resulted in a twofold symmetric pattern with no rolls parallel to the boundaries.

5.2. *Experiments for large Prandtl number* ($10 < \sigma < 20$)

For Prandtl number $\sigma \gtrsim 10$, a different sequence of transitions is observed. As the Rayleigh number is slowly increased through R_c, a pattern of 8 rolls with a weak transverse roll at each end is formed (barely visible as shown in figure 12*a*, but more clearly evident with computer enhancement in figure 13*a*). An asymmetric pattern can also occur at the same Rayleigh number, depending on the history of the flow evolution (figure 13*k*). The successive evolution then depends in detail on the initial pattern. Starting with a symmetric pattern (figure 12*a*, $\sigma = 18$) and heating very slowly ($\mathrm{d}R/\mathrm{d}t < 0.2R_c\ \mathrm{h}^{-1}$), we find that a 'non-soft' 8-roll pattern without transverse rolls at the ends is established by the time the Rayleigh number reaches $7\,R_c$. Near $8\,R_c$, weak cross-rolls are visible near the corners of the container. At $11\,R_c$

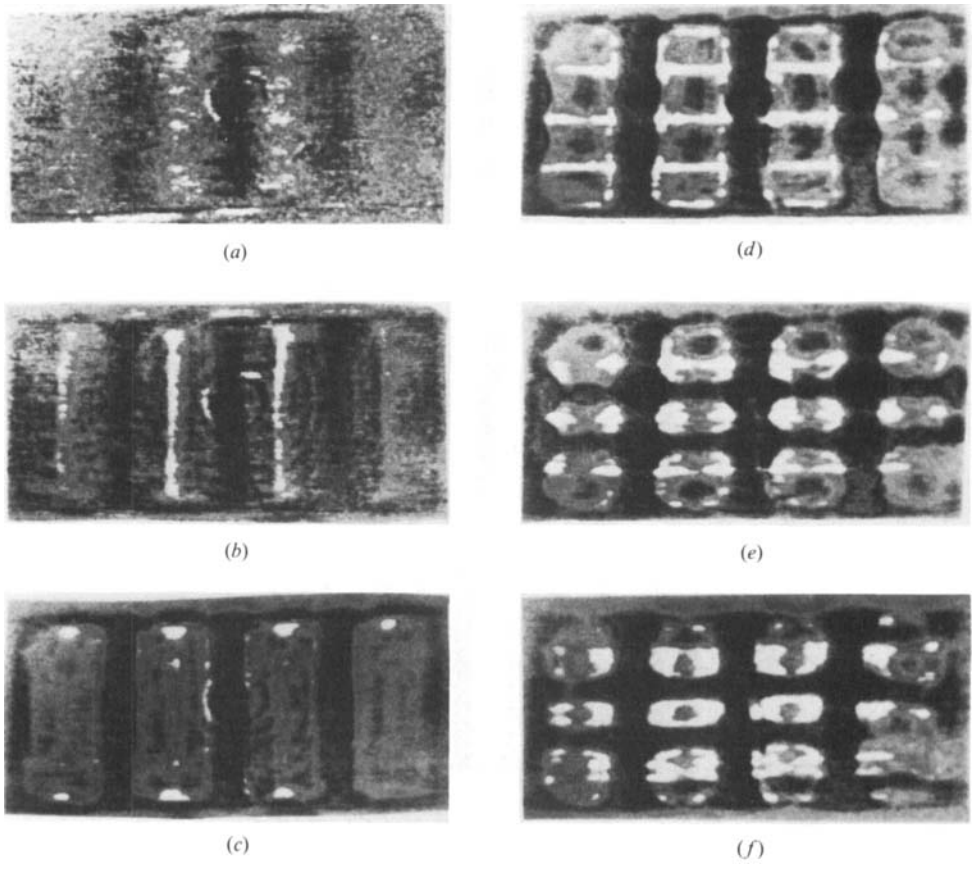

FIGURE 12. Shadowgraph images of the evolution of an 8-roll pattern in container B for $\sigma = 18$. (*a*) $R = 2.3\,R_c$, (*b*) $5.0\,R_c$, (*c*) $11.3\,R_c$, (*d*) $17.5\,R_c$, (*e*) $25.8\,R_c$ and (*f*) $32.6\,R_c$.

(figure 12*c*) the cross-rolls are apparent all along the long edge of the container. These cross-rolls gradually grow in intensity with increasing R, until near $15\,R_c$ they are visible throughout the entire container (figure 12*d*). At $R \approx 32\,R_c$ a slow time-dependent motion is observed near an edge of the pattern, and adjacent bimodal cells at the edge of the pattern begin to 'fuse' together (cf. figure 12*f*). Up to this point the pattern evolution is reversible with decreasing Rayleigh number without any evidence of hysteresis. But, after several horizontal diffusion times, 'fusion' of the bimodal cells begins at the opposite edge of the container, and the pattern becomes significantly distorted. Pattern evolution continues at constant Q_h until the 8-roll pattern has been transformed into a distorted 6-roll pattern, similar to that illustrated in figure 14*d*. Rapid time-dependent motion is then observed throughout the container; the motion is non-periodic, with frequency components comparable to the characteristic frequency for a fluid element to circulate around in a roll. Busse & Whitehead (1974) and Bergé (1981) have reported similar observations of the onset of time dependence associated with 'fusion' of the bimodal cells in a large-aspect-ratio container. In our experiments, however, it appears that the finite aspect ratio imposes a degree of rectangular symmetry which prevents evolution to the complete spatial disorder observed by Busse & Whitehead and Bergé.

As Rayleigh number is increased further, the flow becomes progressively more

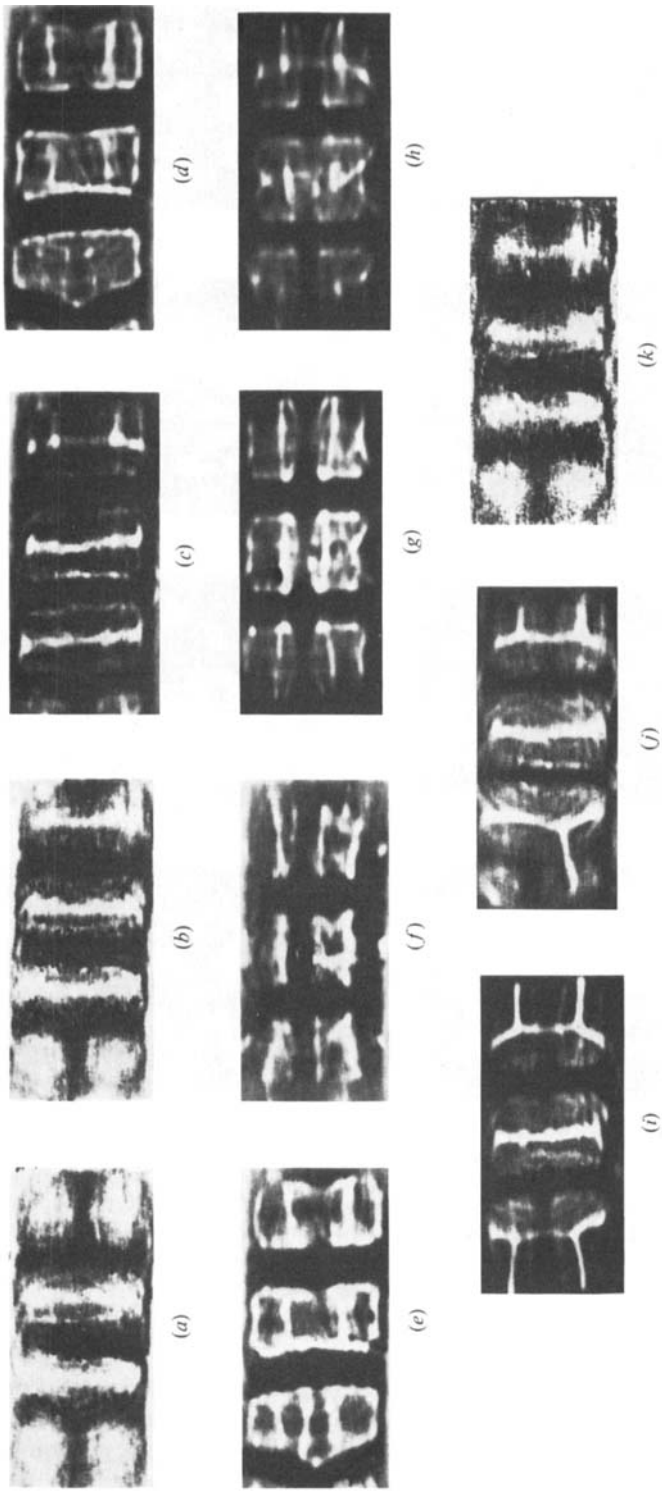

FIGURE 13. Evolution of an 8-roll pattern with 'soft' end rolls in container B for $\sigma = 18$. In the initial pattern, the transverse roll at the right end is slightly longer than that at the left end. (*a*) $R = 2.7\,R_c$, (*b*) $3.2\,R_c$, (*c*) $7.8\,R_c$, (*d*) $14.2\,R_c$, (*e*) $16.4\,R_c$, (*f*) $33.3\,R_c$ (time-dependent), (*g*) $13.4\,R_c$, (*h*) $8.7\,R_c$, (*i*) $5.6\,R_c$, (*j*) $4.3\,R_c$ and (*k*) $2.3\,R_c$.

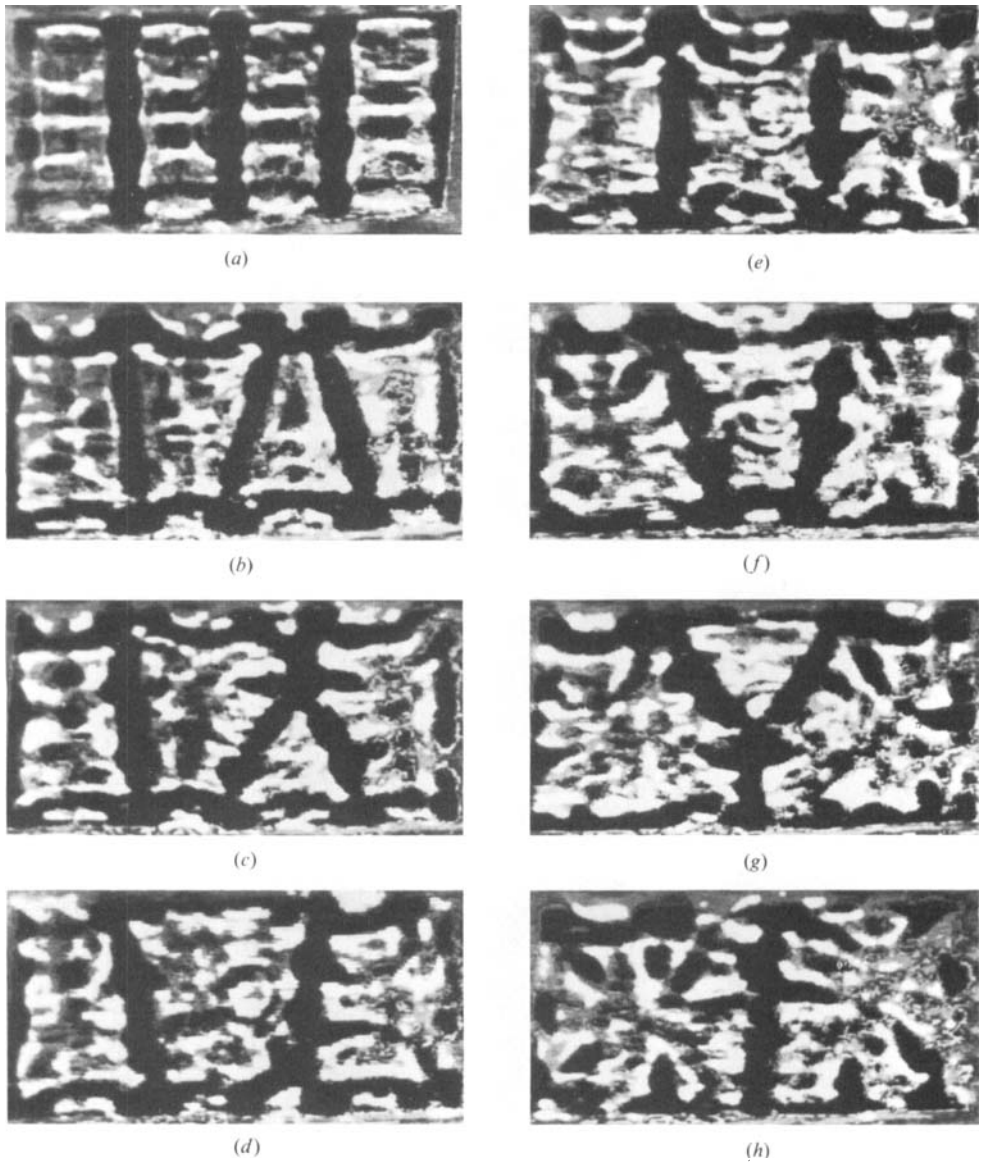

FIGURE 14. Wavenumber transitions above the cross-roll instability boundary in container B for $\sigma = 11$. Times are measured from the onset of convection. (*a*) $R = 27.5\,R_c$, $t = 2{:}30$ (h:min); (*b*) $43.0\,R_c$ at 8:00; (*c*) $43.1\,R_c$ at 8:06; (*d*) $43.2\,R_c$ at 8:08; (*e*) $44.2\,R_c$ at 8:12; (*f*) $46.8\,R_c$ at 8:54; (*g*) $46.9\,R_c$ at 9:06; and (*h*) $46.8\,R_c$ at 9:10. Frames (*b*)–(*d*) and (*f*)–(*h*) are at constant heater power. The flow becomes strongly time-dependent (turbulent) above $30\,R_c$ as evidenced by the complicated structures in the shadowgraph images; however, the basic roll structure is still well defined (roll boundaries are visible as broad dark lines).

turbulent, but the roll boundaries remain well defined, if not always stationary. Above $45\,R_c$ the roll boundaries begin to vary slowly in position and angular orientation. As R is increased from 59 to $63\,R_c$ the roll boundaries adjust in a seemingly random fashion to a smaller mean wavenumber until there is a single upflow boundary near the centre of the container; on the average the upflow boundary is parallel to the short walls of the container (similar to figure 14*h*). With decreasing Rayleigh number

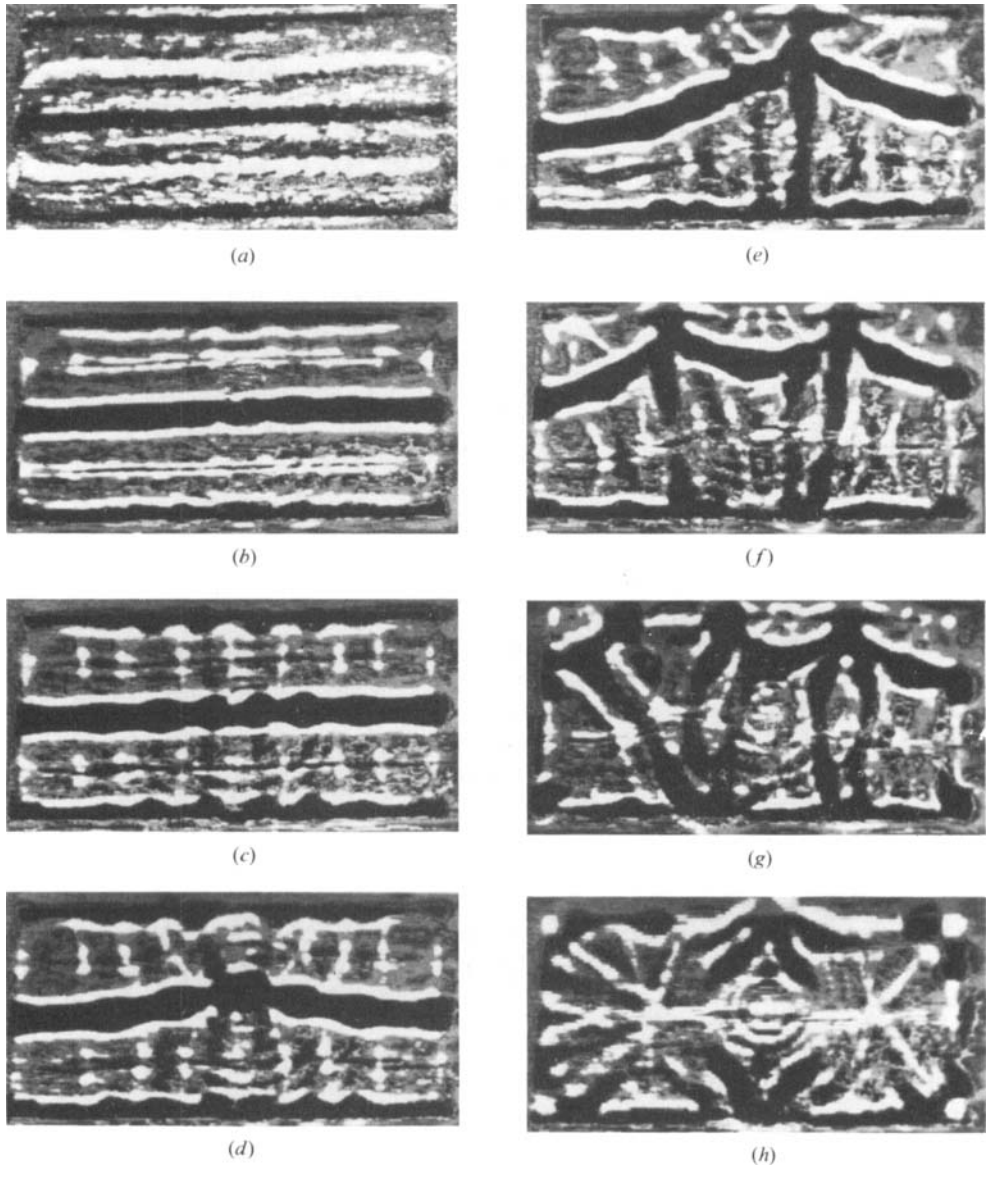

FIGURE 15. Evolution of a pattern of long rolls in container B for $\sigma = 11$. Times are measured from onset of convection. (*a*) $R = 4.7\,R_c$, $t = 15{:}00$ (h:min); (*b*) $20.2\,R_c$ at 25:00; (*c*) $26.2\,R_c$ at 27:27; (*d*) $26.7\,R_c$ at 27:37; (*e*) $27.0\,R_c$ at 27:52; (*f*) $27.1\,R_c$ at 28:02; (*g*) $28.9\,R_c$ at 28:17; (*h*) $29.5\,R_c$ at 28:47. Frames (*c*)–(*f*) and (*g*), (*h*) are at constant heater power. After the break-up of the rolls, (*e*), the flow is strongly time-dependent.

there is a gradual decrease in mean wavenumber, but the flow pattern remains asymmeric until the 8-roll pattern returns very near R_c.

At somewhat lower Prandtl number (e.g. figure 14, $\sigma = 11$), the underlying 8-roll pattern persists well beyond the onset of time dependence. Near $43\,R_c$ (figure 14*b*) there begins a slow, large-amplitude 'breathing' motion of the roll boundaries (figures 14*a* and *b* illustrate different phases of this breathing motion). Then a pair of rolls is removed from the container while heat flux is maintained constant (figures 14*b–d*) in the same manner as observed for smaller Prandtl number. Finally,

at $R \approx 47R_c$ another pair of rolls is removed from the turbulent flow. Although the flow is strongly time-dependent, there still persists a well-defined up-flow roll boundary at the centre of the container (figure 14*h*). Once the second pair of rolls has dissolved near 47 R_c, however, the flow remains time-dependent down to $\approx 10\,R_c$; the pattern still continues to evolve as the Rayleigh number is decreased until an 8-roll pattern with 'soft' ends observed below $2\,R_c$. It is typical that this kind of soft pattern is observed at small Rayleigh number.

The evolution just illustrated with figures 12 and 14 started with a symmetric pattern near R_c. If we begin instead by generating an asymmetric pattern near R_c, the evolution is significantly different. The pattern in figure 13(*a*) is slightly asymmetric, and the asymmetry grows with increasing Rayleigh number (figure 13*b*). Weak cross-rolls are first observed in the corners near $7\,R_c$. Near $16\,R_c$ there is a transition in which the 'soft' roll is removed, leaving a simple 6-roll pattern with fully developed cross-rolls. This pattern becomes locally time-dependent near $27\,R_c$ (figure 13*f*). Above $45\,R_c$ the evolution of the 6-roll pattern is the same as described above.

If we begin slowly decreasing the Rayleigh number again while the 6-roll pattern is still stable (i.e. below $45\,R_c$), the cross-rolls begin to fade near $12\,R_c$, and bimodal convection is gradually replaced by a pattern with soft end rolls (figure 13*h*). As R is decreased further, a series of transitions (figures 13*i–k*) carries the pattern back to the initial pattern (figure 13*b*) below $2.5\,R_c$, or to the symmetric 'soft' pattern (figure 12*a*). Near R_c a continuous variation of the left–right symmetry – e.g. as illustrated by figures 13*a* (nearly symmetric), 13*b* (asymmetric) and 13*k* (intermediate between 13*a* and 13*b*) – seems to be possible depending on flow history, the rate of change of Rayleigh number, and the Prandtl number (i.e. influence of the zigzag instability, cf. figure 2).

The onset of the cross-roll instability for rolls parallel to the long dimension of the container is illustrated in figure 15. Time dependence is initiated with the break-up of the parallel roll pattern (figures 15*d–f*). Note that the final pattern which evolves from the break-up (figure 15*h*) is similar to that which derives at higher Rayleigh number from the initial 8-roll pattern (figure 14*h*). As R is decreased quasi-statically toward R_c, the flow pattern re-anneals to 8 short rolls.

6. Discussion of results

The experimental observations reported in §5 fit remarkably well into the framework of the two-dimensional stability theory, provided one makes plausible allowances for the experimental imposition of finite lateral boundaries. The major influence of the sidewalls, illustrated in that section, has been to shift the boundaries in Rayleigh-number, Prandtl-number, wavenumber space of the various instabilities studied by Busse & Clever (1979); Clever & Busse (1974); Busse (1978); Bolton, Busse & Clever (1983) and Busse & Whitehead (1971, 1974).

6.1. *Occurrence of soft patterns*

Near the onset of convection in container B (aspect ratio 9.3×4.4),† we normally observe a pattern of 8 parallel rolls with soft end rolls. As the Rayleigh number is increased, there is a gradual transition to a non-soft 8-roll pattern; the transition is not well defined in Rayleigh number. For $R < 2\,R_c$, we also oberved what appears to be evidence of zigzag instability. For example, close to R_c the patterns of 6 short

† Our study of patterns close to R_c was confined primarily to container B.

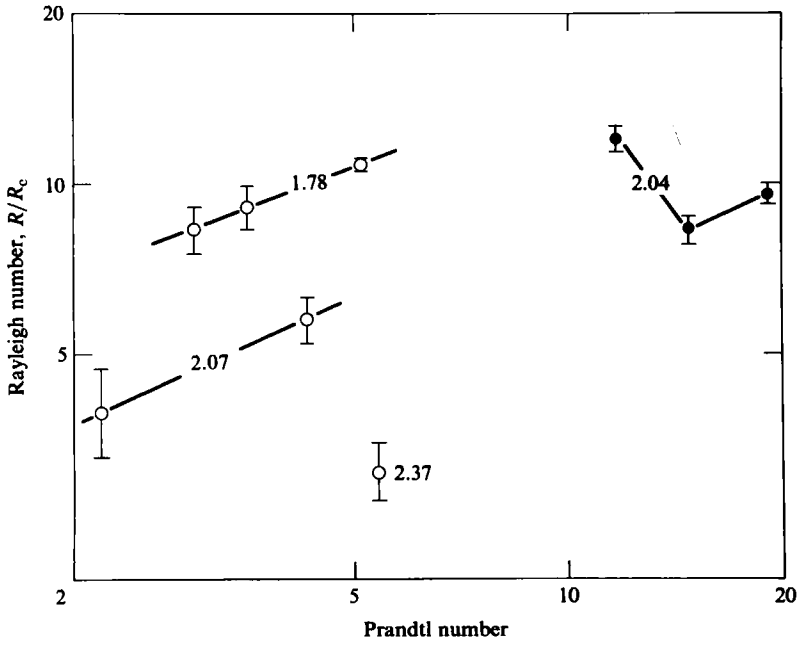

FIGURE 16. Rayleigh number *versus* Prandtl number for transitions to 'soft' end rolls with decreasing Rayleigh number. Values of *initial* mean roll wavenumber are indicated. Container A with water, ○; container B with ethanol, ●.

rolls and 4 long rolls are observed to be unstable to the soft 8-roll pattern as illustrated in figure 13. Figure 16 indicates the observed transitions from parallel rolls to soft patterns with decreasing Rayleigh number. Note that the transition Rayleigh number depends strongly on both the Prandtl number and the initial roll wavenumber. These dependences are consistent with the predictions of the theory for infinite aspect ratio discussed above, but the experimental Rayleigh numbers are about 2 to 3 times as high as expected from the theory.

In numerical calculations using the amplitude equations, Greenside & Coughran (1984) have observed 'soft' patterns near R_c as predicted by Pomeau & Zaleski (1981). In the simulations, short cross-rolls of the critical wavenumber appear at the end boundaries of the container very close to R_c, and penetrate a horizontal distance of order $\epsilon^{-\frac{1}{2}}$ into the fluid, where $\epsilon \equiv (R/R_c - 1)$. This boundary-induced cross-roll instability may be relevant to our observations of soft patterns for $\epsilon \ll 1$, but the theory is not applicable to the observations for $\epsilon \gtrsim 1$ summarized in figure 16.

The studies of Busse & Whitehead (1971) demonstrated that the cross-roll instability has somewhat different manifestations, depending on whether the Rayleigh number is above or below the region of stable two-dimensional convection. At small Rayleigh number the cross-roll instability far away from the boundaries in a large-aspect-ratio container appears as patches of rolls with orientation perpendicular to that of the initial parallel-roll pattern, and the cross-rolls have wavenumber $\tilde{\alpha}$ close to the critical wavenumber (3.114) for onset of two-dimensional convection. Busse & Whitehead reported observations of such cross-roll patterns which are locally similar to our soft patterns. If the cross-roll instability is the origin of the soft patterns which we observe, then the effect of finite aspect ratio appears to be an upward shift of the instability boundary relative to that plotted in figure 1. At large Rayleigh

number the cross-roll instability appears as bimodal convection, which will be discussed in §6.3.

6.2. *Roll-number transitions*

The roll-number transitions observed in our experiments appear to be a manifestation of the long-wavelength skewed-varicose instability and the knot instability predicted by Busse & Clever (1979) for infnite aspect-ratio containers and $10^{-2} \lesssim \sigma \lesssim 10^2$.† According to theory, these instabilities have no intrinsic time dependence, but the two-dimensional parallel-roll pattern becomes unstable to three-dimensional perturbations. Experiments at large aspect ratio, $\Gamma \approx 40$–150 (Busse & Whitehead 1974), have demonstrated that these instabilities continues to grow until the pattern is completely disorganized and exhibits chaotic time-dependent behaviour. Subsequent experiments in smaller containers ($\Gamma < 35$) have also attributed the onset of time dependence to the skewed-varicose instability (Behringer, Gao & Shaumeyer 1983; Gollub, McCarriar & Steinman 1982; Walden 1983).

In our experiments, however, the finite lateral boundary conditions impose a rectangular symmetry which tends to stabilize the two-dimensional character of the flow. As the Rayleigh number is increased across the stability boundary, the flow pattern becomes progressively distorted (yet stationary), until a transient reorganization of the pattern occurs. Remarkably, in nearly all cases the result is a stable nearly two-dimensional roll pattern of smaller wavenumber. Figure 17 summarizes the experimentally observed transitions compared with the approximate calculated values of R for the skewed-varicose and knot instabilities. Although present theory does not provide information about the effects of imposing finite lateral boundaries on the skewed-varicose and knot instabilities, it is plausible to expect that onset of a long-wavelength instability will be suppressed to higher Rayleigh number. In all cases the experimental wavenumber and Prandtl-number dependences are qualitatively consistent with the skewed-varicose and knot instabilities.

6.3. *Bimodal convection*

At large Prandtl number ($\sigma \gtrsim 10$), when the cross-roll instability is encountered at large Rayleigh number, it appears as an instability of the thermal boundary layers near the top and bottom of the fluid layer. A two-dimensional rectangular lattice of rolls (bimodal convection) is observed with weak cross-rolls superimposed on the original convective rolls (Busse & Whitehead 1971). The wavenumber of the cross-rolls increases with increasing Rayleigh number. At larger Rayleigh number, the time-independent bimodal convection becomes oscillatory or undergoes a transition to a more complex pattern, presumably in response to higher-order instabilities (Busse & Whitehead 1974; Whitehead & Chan 1976). In our experiments the onset of bimodal convection with increasing Rayleigh number is a very gradual transition in which weak cross-rolls first appear at the corners of the convection container; then at higher Rayleigh numbers the cross-rolls grow to fill the entire container. Since the definition of the onset of the instability is rather subjective, we have chosen to indicate both the appearance of the corner cross-rolls (denoted by the error bars) in figure 18 and the later appearance of full bimodal convection ($\triangle$). For $\alpha = 2.84$ and 2.72 the appearance of full bimodal convection nearly coincides with the cross-roll instability of the stability theory for infinite aspect ratio.

† Many experiments using large-aspect-ratio containers have reported a decrease in mean roll wavenumber with increasing Rayleigh number. In one instance (Gollub & McCarrier 1982) the observed dependence has been attributed to the skewed-varicose instability.

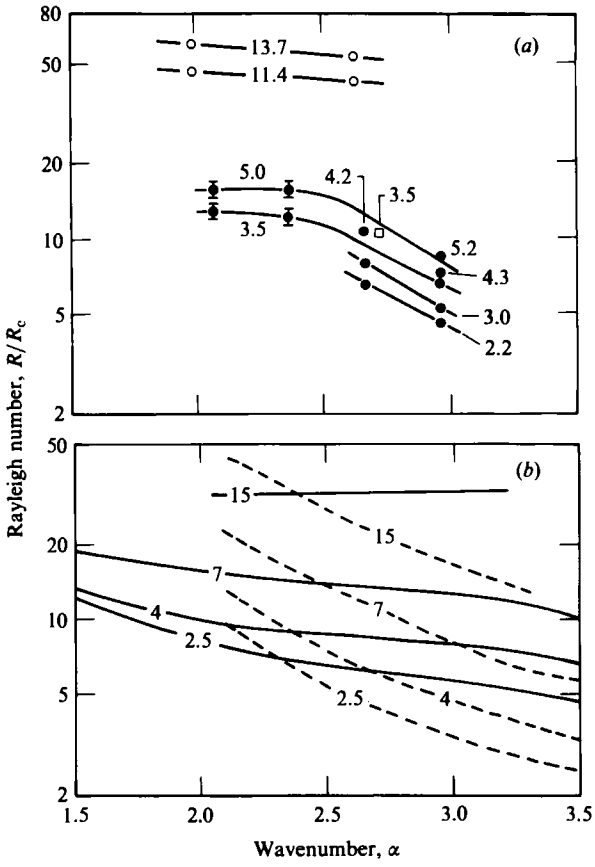

FIGURE 17. Rayleigh number of transitions in roll number as a function of mean roll wavenumber. (*a*) Measured values for patterns of rolls parallel to the short side of the container. Prandtl numbers are indicated; solid lines are meant only to guide the eye. Mean wavenumber plotted is that *prior* to the transition (in which a roll or roll pair is removed from the container). Container A filled with water, ○; container B with ethanol, ●; container B with water, □. (*b*) Theoretical stability boundaries assuming infinite lateral boundary conditions for skewed-varicose (dashed lines) and knot (solid lines) instabilities. Prandtl numbers are indicated. (Note that the experimental data appear to reflect the cross-over of the knot and skewed-varicose instabilities.)

For the small-wavenumber case, $\alpha = 2.04$, things are more complicated. According to theory, for Prandtl numbers $\gtrsim 15$, two-dimensional convection at this wavenumber is unstable to the cross-roll instability for all Rayleigh numbers. Thus, for $\sigma = 19$, there is a gradual transition from the soft end rolls near the onset of convection to fully developed bimodal convection at large Rayleigh number. For $\sigma = 15$, the transition from a soft pattern to bimodal convection is more clearly defined, but there is no range of Rayleigh numbers for which purely two-dimensional convection is observed.

The wavenumber $\tilde{\alpha}$ of the bimodal cross-rolls increases with increasing Rayleigh number and decreases with increasing Prandtl number. Our observations are qualitatively consistent with the studies of Busse & Whitehead (1971); however, a satisfactory quantitative comparison is not possible for two reasons: first, the calculations of Busse & Whitehead were taken in the limit of infinite Prandtl number and did not consider Prandtl-number dependence; secondly, their experiments were

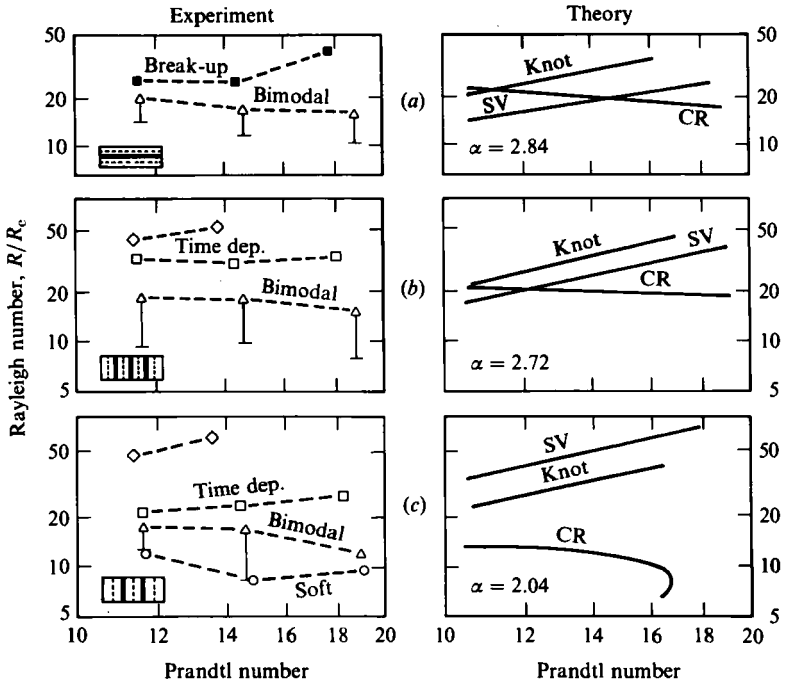

FIGURE 18. Rayleigh number *versus* Prandtl number for the onset of various instabilities in container B. The *initial* patterns are (*a*) 4 rolls parallel to the long side of the container, $\tilde{\alpha} = 2.84$; (*b*) 8 parallel rolls, $\tilde{\alpha} = 2.72$; and (*c*) 6 parallel rolls, $\tilde{\alpha} = 2.04$. △, cross-rolls visible throughout the cell (bimodal convection) (the bottom of the error bars indicates the appearance of cross-rolls at corners of the container); ○, transition to 'soft' end rolls with decreasing Rayleigh number; □, onset of time dependence, in some cases accompanied by ■, break-up of parallel roll boundaries into a complicated flow pattern; ◇, transition to greater wavenumber (pattern is strongly time-dependent before and after transition, but roll boundaries are still well defined). The broken curves are from theory assuming infinite lateral boundary conditions (see *note*, figure 1). Knot = knot instability, CR = cross-roll and SV = skewed-varicose.

at high Prandtl number ($\sigma = 100$). In addition, in many instances $\tilde{\alpha}$ was not well defined in our experiments; for instance, there was often non-uniform spacing between cross-rolls. With increasing Rayleigh number, transitions in wavenumber sometimes occurred by the gradual growth of a new cross-roll pair between existing cross-rolls. For experiments with 4 long rolls, adjustment of $\tilde{\alpha}$ with increasing R occurred by stretching at the end cross-rolls until finally a new pair of cross-rolls was nucleated near one end. There was not a reverse transition with decreasing Rayleigh number; the centre rolls gradually faded with decreasing R.

6.4. *Onset of time dependence*

Bolton, Busse & Clever (1983) have predicted a series of time-dependent instabilities with well-defined frequencies which are expected to occur at sufficiently small α and large Rayleigh number (see figure 1). For small Prandtl numbers ($2.2 \leqslant \sigma \leqslant 5.5$), the observed onset of time dependence (cf. figure 19) appears to be consistent with their predictions in that the time dependence manifests itself as oscillations at the relatively high frequency characteristic of a typical fluid element advecting around in a roll. In addition the wavenumber and Prandtl-number dependences of the threshold Rayleigh number R_t for the onset of time dependence are qualitatively

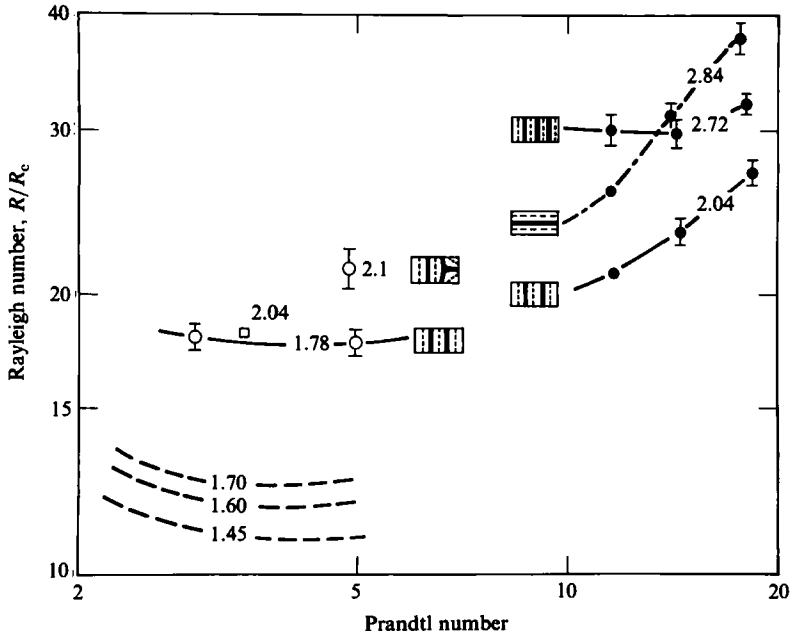

FIGURE 19. Rayleigh number of the onset of time dependence *versus* Prandtl number. Initial *mean* wavenumbers are indicated; note that patterns are sometimes significantly distorted from parallel rolls at the onset of time dependence, however. Container A filled with water, ○; container B with ethanol, ●; container B with water, □. The dashed lines are contours of the oscillatory instability (first odd mode) assuming infinite lateral boundary conditions. Mean wavenumbers are indicated on the contours. (See *note*, figure 1.)

correct. The observed values of R_t are about 40% larger than those predicted, but this may be due to finite-aspect-ratio effects.

The finite-frequency instabilities of Bolton *et al.* have different frequencies in different parts of the container when the flow pattern is distorted from a set of parallel rolls (Walden *et al.* 1984). Thus the spatial pattern is very closely related to time dependence. This effect appears to determine the number of incommensurate frequencies which can appear before the onset of chaos. In the experiments described here, as many as five incommensurate frequencies have been observed simultaneously without chaos. Since similar behaviour is not observed in very large or very small containers, the regime of aspect ratio discussed here provides us with a new and interesting regime in which to study the onset of time dependence and the approach to chaos.

For Prandtl numbers greater than about 5, these oscillatory instabilities are preceded by other instabilities for all wavenumbers. For example, for high Prandtl number, the cross-roll instability (and bimodal convection) is encountered prior to the onset of time dependence. Busse & Whitehead (1971, 1974) have investigated experimentally and theoretically the cross-roll instability and the onset of time dependence for large Prandtl number. In this case, time dependence occurs as an oscillatory instability of the cross-rolls, which will be described in the next section.

6.5. *Higher-order instabilities*

As discussed above, the onset of time dependence for $\sigma \gtrsim 10$ occurs as an oscillatory instability of the cross-rolls or as a collective instability which leads immediately to

a transition in the flow pattern and chaotic time-dependent behaviour. The 'collective instability' observed by Busse & Whitehead (1974) is so named because in containers of large aspect ratio it grows from bimodal convection by 'collecting' between three and six bimodal cells into one large cell of 'spoke-like' appearance,† much like those in figure 14*h* or 15*h*. However, two-dimensional stability theory does not provide information about this instability since it arises from a three-dimensional flow pattern. The Rayleigh number R_t for onset of time dependence is a strong function of three parameters: Prandtl number, roll wavenumber α, and cross-roll wavenumber $\tilde{\alpha}$. Again, the limited parameter range of the study by Busse & Whitehead (1974) and the substantial uncertainty in determination of $\tilde{\alpha}$ in our experiments do not permit a satisfactory quantitative comparison of their theory and experiments with our results. In general, the values of R_t estimated from Busse & Whitehead (1974) were 10–20% greater than our experimental values, and the dependence of R_t on σ, α and $\tilde{\alpha}$ appears to be consistent with their predictions in that R_t increases with increases in each of these parameters.

For the parameter range of our experiments, it appears that both the knot and skewed-varicose instabilities can influence a pattern transition to a smaller number of rolls even for three-dimensional flows caused by other instabilities. For example, in experiments at high Prandtl number we have seen similar transitions in the flow pattern, even though convection is strongly time dependent and far beyond the cross-roll instability. Because the underlying flow pattern still has a degree of rectangular symmetry, it appears that the skewed-varicose and knot instabilities are still in some fashion relevant. This is confirmed by Prandtl-number and wavenumber dependence of the transition Rayleigh number consistent with the predictions of two-dimensional stability theory and our observations at lower Prandtl number (cf. figure 17).

7. Concluding remarks

In this paper we have studied the mechanisms which determine pattern selection in a rectangular container having approximate aspect ratio 10×5, which we have characterized as finite but not small. The transitions between flow patterns occur at Rayleigh numbers and wavenumbers which correspond qualitatively to the predictions of the theory for an infinite system of parallel rolls (Busse & Clever 1979; Clever & Busse 1974; Busse 1974; Bolton, Busse & Clever 1983; Busse & Whitehead 1971, 1974). The long-wavelength skewed-varicose and knot instabilities are found to be suppressed by the finite aspect ratio to Rayleigh numbers about 30% higher than those predicted for infinite aspect ratio. On the other hand, the onset of the cross-roll instability seems to be enhanced by the finite boundary conditions, with bimodal convection occurring at the corners of the container at somewhat lower Rayleigh numbers than those predicted for infinite aspect ratio. This correspondence between the results for finite-aspect-ratio containers and the theory assuming infinite aspect ratio gives hope that one might be able to treat the stability of patterns of parallel rolls in a moderate-sized rectangular container by a perturbation of the stability analysis for the infinite-aspect-ratio case.

In the experiments reported here, the skewed-varicose and knot instabilities are found to trigger successive transitions between time-independent flow patterns. This contrasts with behaviour observed in much larger containers where, at the first onset

† Such 'spoke-pattern' convection in large-aspect-ratio containers is described by Busse & Whitehead (1974); it appears to be related to the knot instability (Busse 1981).

of the skewed-varicose (or knot) instability, the flow pattern evolves to a complicated and ever-changing three-dimensional pattern of rolls. The boundary-induced stabilization of an almost two-dimensional roll pattern in the present experiments has also allowed us to study the transition to time dependence in a region of Rayleigh-number and wavenumber space where we are able to observe the new time-dependent instabilities recently predicted by Bolton, Busse & Clever (1983).

The data presented here raise a number of questions about Rayleigh–Bénard convection in finite-aspect-ratio containers. Since we are able to stabilize to much larger Rayleigh number the wandering of the rolls (which is observed in larger containers at $R \lesssim 5R_c$), we are able to observe several transitions in the flow pattern with increasing Rayleigh number before the onset of time dependence. It would now be of interest to understand in a more quantitative way the regimes of aspect ratios where the system behaves in a different manner (i.e. mimicking the behaviour observed in very large or very small containers).

We wish to acknowledge helpful discussions with E. W. Bolton, F. H. Busse, M. C. Cross, H. S. Greenside, P. C. Hohenberg and J. Tesauro, and the extensive technical assistance of G. Dimino and N. Hartsough.

REFERENCES

AHLERS, G. 1980 Effect of departures from the Oberbeck–Boussinesq approximation on the heat transport of horizontal convecting fluid layers. *J. Fluid Mech.* **98**, 137–148.

BEHRINGER, R. P., GAO, H. & SHAUMEYER, J. N. 1983 Time dependence in Rayleigh–Bénard convection with a variable cylindrical geometry. *Phys. Rev. Lett.* **50**, 1199–1202.

BERGÉ, P. 1981 Rayleigh–Bénard convection in high Prandtl number fluids. In *Chaos and Order in Nature* (ed. H. Haken), pp. 14–24. Springer.

BOLTON, E. W., BUSSE, F. H. & CLEVER, R. M. 1983 An antisymmetric oscillatory instability of convection rolls. *Bull. Am. Phys. Soc.* **28**, 1399.

BUSSE, F. H. 1967*a* The stability of finite amplitude cellular convection and its relation to an extremum principle. *J. Fluid Mech.* **30**, 625–649.

BUSSE, F. H. 1967*b* On the stability of two-dimensional convection in a layer heated from below. *J. Maths & Phys.* **46**, 140–149.

BUSSE, F. H. 1978 Non-linear properties of thermal convection. *Rep. Prog. Phys.* **41**, 1929–1967.

BUSSE, F. H. 1981 Transition to turbulence in Rayleigh–Bénard convection. In *Hydrodynamic Instabilities and the Transition to Turbulence* (eds. H. L. Swinney & J. P. Gollub), pp. 97–137. Springer.

BUSSE, F. H. & CLEVER, R. M. 1979 Instabilities of convection rolls in a fluid of moderate Prandtl number. *J. Fluid Mech.* **91**, 319–335.

BUSSE, F. H. & WHITEHEAD, J. A. 1971 Instabilities of convection rolls in a high Prandtl number fluid. *J. Fluid Mech.* **47**, 305–320.

BUSSE, F. H. & WHITEHEAD, J. A. 1974 Oscillatory and collective instabilities in large Prandtl number convection. *J. Fluid Mech.* **66**, 67–79.

CHEN, M. M. & WHITEHEAD, J. A. 1968 Evolution of two-dimensional periodic Rayleigh–Bénard convection cells of arbitrary wave numbers. *J. Fluid Mech.* **31**, 1–15.

CLEVER, R. M. & BUSSE, F. H. 1974 Transition to time-dependent convection. *J. Fluid Mech.* **65**, 625–645.

DUBOIS, M. & BERGÉ, P. 1980 Experimental evidence for the oscillators in a convective biperiodic regime. *Phys. Lett.* **76** A, 53–56.

GAO, H. & BEHRINGER, R. P. 1984 Onset of convective time dependence in cylindrical containers. *Phys. Rev.* A **30**, 2837–2839.

GOLLUB, J. P. & BENSON, S. V. 1980 Many routes to turbulent convection. *J. Fluid Mech.* **100**, 449–470.

GOLLUB, J. P. & MCCARRIAR, A. R. 1982 Convection patterns in Fourier space. *Phys. Rev.* **A 26**, 3470–3476.

GOLLUB, J. P., MCCARRIAR, A. R. & STEINMAN, J. F. 1982 Convective pattern evolution and secondary instabilities. *J. Fluid Mech.* **125**, 259–281.

GREENSIDE, H. S. & COUGHRAN, W. M. 1984 Nonlinear pattern formation near the onset of Rayleigh–Bénard convection. *Phys. Rev.* **A 30**, 398–428.

MAURER, J. & LIBCHABER, A. 1980 Effect of the Prandtl number on the onset of turbulence in liquid 4-He. *J. Physique Lett.* **41**, L515–L518.

MUELLER, K. H., AHLERS, G. & POBELL, F. 1976 Thermal expansion coefficient, scaling, and universality near the superfluid transition of 4-He. *Phys. Rev.* **B 14**, 2096–2118.

POMEAU, Y. & ZALESKI, S. 1981 Wavelength selection in one-dimensional cellular structures. *J. Physique* **42**, 515–528.

WALDEN, R. W. 1983 Some new routes to chaos in Rayleigh–Bénard convection. *Phys. Rev.* **A 27**, 1255–1258.

WALDEN, R. W. & AHLERS, G. 1981 Non-Boussinesq and penetrative convection in a cylindrical cell. *J. Fluid Mech.* **109**, 89–114.

WALDEN, R. W., KOLODNER, P., PASSNER, A. & SURKO, C. M. 1984 Nonchaotic Rayleigh–Bénard convection with four and five incommensurate frequencies. *Phys. Rev. Lett.* **53**, 242–245.

WHITEHEAD, J. A. & CHAN, G. L. 1976 Stability of Rayleigh–Bénard convection rolls and bimodal flow at moderate Prandtl numbers. *Dyn. Atmos. Oceans* **1**, 33–49.